Novel 3-D Non-Stationary Wideband Models for Massive MIMO Channels

Carlos F. López and Cheng-Xiang Wang, *Fellow, IEEE*

***Abstract*— In this paper, a novel 3-D non-stationary wideband geometry-based stochastic theoretical channel model for massive multiple-input multiple-output communication systems is proposed. First, a second-order approximation to the spherical wavefront in space and time domains, i.e., *parabolic wavefront*, is proposed to efficiently model *near-field effects*. Second, *environment evolution* effects are modeled by spatial-temporal cluster (re)appearance and shadowing processes. We propose (re)appearance processes to model the visibility of clusters with enhanced spatial-temporal consistency. Shadowing processes are used to capture smooth spatial-temporal variations of the clusters' average power. In addition, a corresponding simulation model is derived along with a 3-D extension of the Riemann sum method for parameters computation. Key statistical properties of the proposed model, e.g., the spatial-temporal cross-correlation function, are derived and analyzed. Finally, we present numerical and simulation results showing an excellent agreement between the theoretical and simulation models and validating the proposed parameter computation method. The accuracy and flexibility of the proposed simulation model are demonstrated by comparing simulation results and measurements of the delay spread, slope of cluster power variations, and visibility regions' size.**

***Index Terms*— Massive MIMO, 3D non-stationary channel model, parabolic wavefront, cluster reapperance, shadowing of clusters.**

I. Introduction

In RECENT years, massive multiple-input multiple-output (MIMO) technology has been proposed as a key enabler for the fifth generation (5G) wireless communication systems due to its promising capabilities to efficiently cope with an increasing number of devices and high data traffic demand [1]–[3]. In spite of the great challenges the use of a large number of antennas entails, recent research demonstrated that most benefits claimed from the early theoretical studies on massive MIMO, e.g., increase of capacity and efficiency, are achievable in realistic conditions [4]–[6].

In order to exploit important benefits of massive MIMO technologies, the distance between the antenna elements of the array cannot be reduced as much as desired [7]. Consequently, massive MIMO communication systems using a large number of antennas may result in arrays that span long distances, and hence they may experience new propagation effects, e.g, *near-field* and *environment evolution* effects.

Near-field effects are caused by users or scatterers lying within the Fresnel region of the array, which is delimited by the Rayleigh distance, i.e., $2D_A^2/\lambda$ with λ and D_A denoting the wavelength and the maximum dimension of the array, respectively. In near-field conditions, the channel cannot be regarded as wide-sense stationary (WSS) because channel parameters such as the angles of arrival/departure (AoA/AoD) and the Doppler frequency shifts may be different for sufficiently separated antenna elements. The term *environment evolution* refers to the variations in the large-scale properties of the channel with which the signals from different antenna elements interact. Since the signal transmitted or received by sufficiently separated antenna elements is scattered by different sets of objects or clusters, occlusion and shadowing along the array may occur to individual clusters. Both near-field and environment evolution effects were measured in realistic conditions and their impact on the performance of MIMO communication systems was studied in [8]–[14].

As these new effects are usually negligible in conventional MIMO systems, channel models such as those developed in 3GPP-SCM [15], WINNER+ [16], IMT-A [17], COST 2100 [18], and 3GPP-3D [19], are not designed to capture them properly. Nonetheless, recent investigations in massive MIMO channel modeling have proposed solutions such as the spherical wavefront and cluster visibility processes to model near-field and environment evolution effects, respectively [20]. Models like QuaDRiGa [21] and mmMAGIC [22] implemented the spherical wavefronts by updating scatterer parameters for every antenna element and at each time instant, resulting in a high computational complexity. These three-dimensional (3D) geometry-based stochastic models (GBSMs) include cluster birth-death processes and power ramps between stationary segments both over the array and in time domain. However, once a cluster has disappeared, it cannot reappear again with similar characteristics. Thus, clusters occluded for short intervals over the array are considered as multiple independent clusters. This increases the number of clusters per simulation and underestimates the spatial-temporal correlation of the channel in the large scale.

Although COST 2100 model does not support spherical wavefronts for large arrays, it includes a cluster-level evolution approach called *visibility regions* (VRs), i.e., circular regions where clusters of scatterers are visible [18]. Gao *et al.* [9]

Manuscript received May 25, 2017; revised October 2, 2017 and December 15, 2017; accepted January 24, 2018. Date of publication February 13, 2018; date of current version May 8, 2018. This work was supported in part by the EU H2020 5G Wireless Project under Grant 641985, in part by the EU H2020 RISE TESTBED Project under Grant 734325, in part by the EU FP7 QUICK Project under Grant PIRSES-GA-2013-612652, and in part by the EPSRC TOUCAN Project under Grant EP/L020009/1. The associate editor coordinating the review of this paper and approving it for publication was T. G. Pratt. *(Corresponding author: Cheng-Xiang Wang.)*

The authors are with the Institute of Sensors, Signals and Systems, School of Engineering and Physical Sciences, Heriot-Watt University, Edinburgh EH14 4AS, U.K. (e-mail: c.f.lopez@hw.ac.uk; cheng-xiang.wang@hw.ac.uk).

Color versions of one or more of the figures in this paper are available online at http://ieeexplore.ieee.org.

Digital Object Identifier 10.1109/TWC.2018.2804385

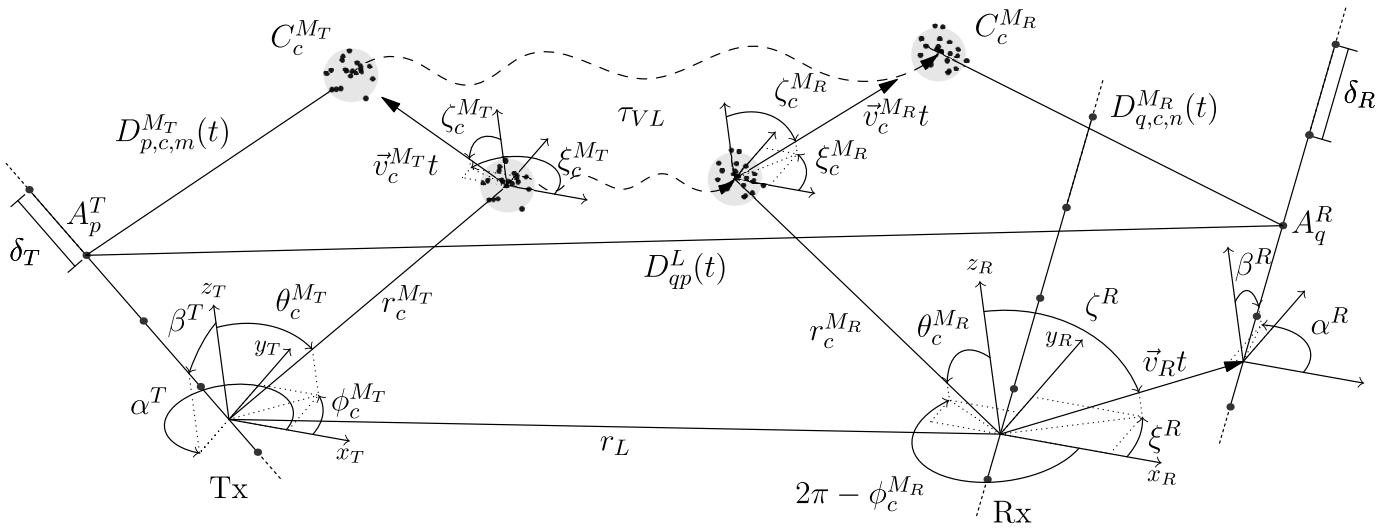

Fig. 1. A 3D wideband massive MIMO channel model.

proposed to use VRs to model clusters' visibility over the array and incorporated a linear model to represent variations of the clusters' average power. However, they neglected to model more accurate variations of this power, i.e., cluster-level shadowing, and did not consider cluster reappearance either.

Wu *et al.* [23], [24] developed two-dimensional (2D) and 3D massive MIMO GBSMs, respectively, including spherical wavefronts and cluster (dis)appearance similarly to QuaDRiGa. However, none of these models included cluster shadowing nor reappearance. Furthermore, the authors used the method of equal areas (MEA) to obtain the simulation model parameters as they considered independent azimuth and elevation AoAs/AoDs, which is generally not the case.

MiWEBA [25] is a quasi-deterministic massive MIMO channel model for millimeter-wave wireless communications based on IEEE 802.11ad model [26]. MiWEBA implemented the spherical wavefront and stochastic ray flashing. However, ray flashing only covers (re)appearance of deterministic rays, neglecting cluster (re)appearance and shadowing. Map-based METIS massive MIMO channel model [27] considered spherical wavefronts by computing the exact propagation paths of rays in the environment with a high computational complexity. Whereas the map-based METIS model used realistic maps to account for environment evolution effects, its stochastic counterpart neglected cluster-level (re)appearance and shadowing.

Previously, we developed a 2D GBSM [28] that can capture near-field effects with reduced complexity using parabolic wavefronts. We also proposed a cluster evolution approach accounting for cluster (re)appearance and smooth power variations over the array. However, this model is limited to small receiving arrays in 2D environments with only multi-bounce clusters (MBCs). Moreover, near-field and environment evolution effects were considered only over the array.

The work presented here extends the model proposed in [28]. In the following we highlight the main **contributions** and novelties of this work:

1) We extend the parabolic wavefront to 3D space and time domain. In this model, both the transmitter (Tx) and the receiver (Rx) can be equipped with large antenna arrays.
2) We extend the spatial environment evolution processes to the time domain. First, cluster (re)appearance processes are used to model the visibility of clusters and line-of-sight (LOS) to non-LOS (NLOS) transitions. Second, shadowing processes are used to model smooth variations of the clusters' average power over the array and time domains more accurately.
3) We provide approximate expressions for the relationship between non-stationary properties of the channel, e.g., spatial-temporal Doppler frequency drifts, and the distances between the transmitting and receiving arrays as well as between these arrays and clusters.
4) We propose a 3D extension of the Riemann sum method (RSM) [29] to compute the amplitude and angular parameters of the 3D simulation model and use the von Mises-Fisher (VMF) distribution to jointly model the azimuth and elevation angles of the scatterers.

The rest of this paper is organized as follows. In Section II, a theoretical non-stationary wideband massive MIMO channel model is proposed. In this section, the parabolic wavefront and cluster-level evolution processes are described. Statistical properties of the theoretical model, e.g., the spatial-temporal cross-correlation function (ST-CCF), are derived in Section III. In Section IV, a corresponding simulation model and its statistical properties are derived, along with the new parameter computation method proposed. The excellent agreement between the theoretical and simulation model results is presented in Section V along with a comparison of simulation results and measurements. Finally, conclusions are drawn in Section VI.

Notation: Sets are indicated as $\mathcal{Z} = \{\}$. A scalar h_{qp} denotes the (q,p)-th element of a matrix $\mathbf{H}$. Vectors are indicated with an arrow such as $\vec{v}$.

II. A Theoretical Non-Stationary Wideband Massive MIMO Channel Model

Let us consider a 3D channel model represented in Fig. 1 where the uniform linear array (ULA) at the Tx or base station is composed of N_{T} equally δ_{T}-spaced antenna elements oriented by the elevation and azimuth angles β^{T} and α^{T},

TABLE I
DEFINITION OF PARAMETERS OF THE MASSIVE MIMO CHANNEL MODEL IN FIG. 1

Parameter	Definition
$\delta_{\mathrm{T}}, \delta_{\mathrm{R}}$	Distances between consecutive elements in the transmit- and receive-array, respectively
$r_c^{\mathrm{S_{T(R)}}}, r_c^{\mathrm{M_{T(R)}}}$	Distances from the center of the transmit- (receive-) array to $\mathrm{C}_c^{\mathrm{S_{T(R)}}}$ and $\mathrm{C}_c^{\mathrm{M_{T(R)}}}$, respectively
$D_{p,c,i}^{\mathrm{S_T}}(t)$, $D_{q,c,i}^{\mathrm{S_R}}(t)$	Distances from A_p^{T} to $\mathrm{C}_{c,i}^{\mathrm{S_T}}$ and from A_q^{R} to $\mathrm{C}_{c,i}^{\mathrm{S_R}}$, respectively
$D_{p,c,m}^{\mathrm{M_T}}(t)$, $D_{q,c,n}^{\mathrm{M_R}}(t)$	Distances from A_p^{T} to $\mathrm{C}_{c,m}^{\mathrm{M_T}}$ and from A_q^{R} to $\mathrm{C}_{c,n}^{\mathrm{M_R}}$, respectively
r_{L}	Distance between the centers of the transmit- and the receive-array
$\theta_c^{\ell}, \phi_c^{\ell}$	Elevation and azimuth angles of C_c^{ℓ} with $\ell \in \{\mathrm{S_T}, \mathrm{S_R}, \mathrm{M_T}, \mathrm{M_R}\}$, respectively
$\theta_{c,i}^{\mathrm{S_{T(R)}}}, \phi_{c,i}^{\mathrm{S_{T(R)}}}$	Elevation and azimuth angles of the scatterer $\mathrm{C}_{c,i}^{\mathrm{S_{T(R)}}}$, respectively
$\theta_{c,m(n)}^{\mathrm{M_{T(R)}}}, \phi_{c,m(n)}^{\mathrm{M_{T(R)}}}$	Elevation and azimuth angles of the scatterer $\mathrm{C}_{c,m(n)}^{\mathrm{M_{T(R)}}}$, respectively
$\theta^{\mathrm{L}}, \phi^{\mathrm{L}}$	Elevation and azimuth angles of the Rx with respect to the Tx, respectively
$\zeta_c^{\ell}, \xi_c^{\ell}$	Elevation and azimuth angles of the velocity of C_c^{ℓ} with $\ell \in \{\mathrm{S_T}, \mathrm{S_R}, \mathrm{M_T}, \mathrm{M_R}\}$, respectively
$\zeta^{\mathrm{R}}, \xi^{\mathrm{R}}$	Elevation and azimuth angles of the velocity vector of the Rx, respectively
$\beta^{\mathrm{T(R)}}, \alpha^{\mathrm{T(R)}}$	Elevation and azimuth orientation angles of the transmit (receive) array, respectively
v_c^{ℓ}, v_{R}	Speeds of the cluster C_c^{ℓ} with $\ell \in \{\mathrm{S_T}, \mathrm{S_R}, \mathrm{M_T}, \mathrm{M_R}\}$ and speed of the Rx, respectively

respectively. Similarly, the Rx or mobile station (MS) ULA is composed of N_{R} equally δ_{R}-spaced antenna elements oriented by the elevation and azimuth angles β^{R} and α^{R}, respectively. The pth transmit and qth receive antenna-elements are denoted by A_p^{T} and A_q^{R}, respectively. Moreover, the MS moves at a constant speed v_{R} in the direction indicated by the elevation and azimuth angles ζ^{R} and ξ^{R}, respectively. The signal received at the MS is a superposition of the LOS and scattered components through C_{S} single-bounce clusters (SBCs) and C_{M} MBCs. However, only the cth MBC is represented in the figure for clarity. This cluster is modeled as a one-to-one pair at both sides of the communication link, where the transmit-side MBC is represented as $\mathrm{C}_c^{\mathrm{M_T}}$ and the receive-side MBC as $\mathrm{C}_c^{\mathrm{M_R}}$ for $c = 1, 2, \ldots, C_{\mathrm{M}}$. Every pair of MBCs $\mathrm{C}_c^{\mathrm{M_T}} - \mathrm{C}_c^{\mathrm{M_R}}$ is connected through a virtual link that models the delay as in [18]. Clusters $\mathrm{C}_c^{\mathrm{M_T}}$ and $\mathrm{C}_c^{\mathrm{M_R}}$ are comprised of M_c and N_c scatterers, denoted as $\mathrm{C}_{c,m}^{\mathrm{M_T}}$ for $m = 1, 2, \ldots, M_c$ and $\mathrm{C}_{c,n}^{\mathrm{M_R}}$ for $n = 1, 2, \ldots, N_c$, respectively. Although the cth SBC, denoted as $\mathrm{C}_c^{\mathrm{S}}$, is a single cluster and has a uniquely defined position, it is convenient for notation simplicity to use two representations as $\mathrm{C}_c^{\mathrm{S_T}}$ and $\mathrm{C}_c^{\mathrm{S_R}}$ for $c = 1, 2, \ldots, C_{\mathrm{S}}$, denoting the SBC from the Tx and Rx frames of reference, respectively. The cth SBC $\mathrm{C}_c^{\mathrm{S}}$ is comprised of I_c scatterers whose transmit- and receive-side representations are denoted as $\mathrm{C}_{c,i}^{\mathrm{S_T}}$ and $\mathrm{C}_{c,i}^{\mathrm{S_R}}$ for $i = 1, 2, \ldots, I_c$, respectively. The position vector of a transmit-side SBC scatterer at time t is $\vec{C}_{c,i}^{\mathrm{S_T}}(t) = \vec{C}_{c,i}^{\mathrm{S_T}}(0) + \vec{v}_{c,i}^{\mathrm{S_T}} t$, with

$$\vec{C}_{c,i}^{\mathrm{S_T}}(0) = r_{c,i}^{\mathrm{S_T}}(\sin\theta_{c,i}^{\mathrm{S_T}}\cos\phi_{c,i}^{\mathrm{S_T}}, \sin\theta_{c,i}^{\mathrm{S_T}}\sin\phi_{c,i}^{\mathrm{S_T}}, \cos\theta_{c,i}^{\mathrm{S_T}}) \quad (1)$$

$$\vec{v}_{c,i}^{\mathrm{S_T}} = v_{c,i}^{\mathrm{S_T}}(\sin\zeta_{c,i}^{\mathrm{S_T}}\cos\xi_{c,i}^{\mathrm{S_T}}, \sin\zeta_{c,i}^{\mathrm{S_T}}\sin\xi_{c,i}^{\mathrm{S_T}}, \cos\zeta_{c,i}^{\mathrm{S_T}}) \quad (2)$$

denoting the initial position and velocity vectors of the scatterer, respectively. Similarly, the position vectors of receive-side scatterers are computed as in (1) and (2) by substituting $\mathrm{S_T}$ by $\mathrm{S_R}$. For clarity, the rest of the parameters of the channel model are presented in Table I.

In general, it is assumed that every scatterer within a cluster is approximately at the same distance from the center of the corresponding array and moves with the same velocity, e.g., $r_{c,i}^{\mathrm{S_T}} \approx r_c^{\mathrm{S_T}}$, $v_{c,i}^{\mathrm{S_T}} \approx v_c^{\mathrm{S_T}}$, $\zeta_{c,i}^{\mathrm{S_T}} \approx \zeta_c^{\mathrm{S_T}}$, and $\xi_{c,i}^{\mathrm{S_T}} \approx \xi_c^{\mathrm{S_T}}$. The center of the receive-array with respect to the center of the transmit-array at any time t is $\vec{R}(t) = \vec{R}(0) + \vec{v}_{\mathrm{R}} t$, where

$$\vec{R}(0) = r_{\mathrm{L}}\left(\sin\theta^{\mathrm{L}}\cos\phi^{\mathrm{L}}, \sin\theta^{\mathrm{L}}\sin\phi^{\mathrm{L}}, \cos\theta^{\mathrm{L}}\right) \quad (3)$$

$$\vec{v}_{\mathrm{R}} = v_{\mathrm{R}}\left(\sin\zeta^{\mathrm{R}}\cos\xi^{\mathrm{R}}, \sin\zeta^{\mathrm{R}}\sin\xi^{\mathrm{R}}, \cos\zeta^{\mathrm{R}}\right). \quad (4)$$

The position vector of the transmitting antenna element A_p^{T} from the center of the array is

$$\vec{\delta}_p^{\mathrm{T}} = \delta_p(\sin\beta^{\mathrm{T}}\cos\alpha^{\mathrm{T}}, \sin\beta^{\mathrm{T}}\sin\alpha^{\mathrm{T}}, \cos\beta^{\mathrm{T}}) \quad (5)$$

with $\delta_p = (N_{\mathrm{T}} - 2p + 1)\delta_{\mathrm{T}}/2$ for $p = 1, 2, \ldots, N_{\mathrm{T}}$. The position vector of A_q^{R} from the center of the receive-array can be analogously obtained by substituting T by R and p by q in (5). Finally, it is important to remark that, unlike conventional MIMO channel models, the far-field assumption or Rayleigh criterion, i.e., $r_{\mathrm{L}} \gg \max[2(N_{\mathrm{T}} - 1)^2\delta_{\mathrm{T}}^2, 2(N_{\mathrm{R}} - 1)^2\delta_{\mathrm{R}}^2]/\lambda$ and $r_c^{\ell} \gg \max[2(N_{\mathrm{T}} - 1)^2\delta_{\mathrm{T}}^2, 2(N_{\mathrm{R}} - 1)^2\delta_{\mathrm{R}}^2]/\lambda$ with $\ell \in \{\mathrm{S_T}, \mathrm{S_R}, \mathrm{M_T}, \mathrm{M_R}\}$, is not imposed here.

A. Channel Impulse Response (CIR)

The massive MIMO channel is represented by the matrix $\mathbf{H}(t, \tau) = [h_{qp}(t, \tau)]_{N_{\mathrm{R}} \times N_{\mathrm{T}}}$ for $p = 1, 2, \ldots, N_{\mathrm{T}}$ and $q = 1, 2, \ldots, N_{\mathrm{R}}$. The CIR $h_{qp}(t, \tau)$ is calculated as the superposition of the LOS, SBC, and MBC components as

$$h_{qp}(t, \tau) = h_{qp}^{\mathrm{L}}(t)\delta(\tau - \tau^{\mathrm{L}}) + \sum_{c=1}^{C_{\mathrm{S}}} h_{qp,c}^{\mathrm{SB}}(t)\delta(\tau - \tau_c^{\mathrm{SB}}) + \sum_{c=1}^{C_{\mathrm{M}}} h_{qp,c}^{\mathrm{MB}}(t)\delta(\tau - \tau_c^{\mathrm{MB}}) \quad (6)$$

where the superscripts L, SB, and MB refer to LOS, SBC, and MBC components, respectively. The propagation delays $\tau^{\mathrm{L}}, \tau_c^{\mathrm{SB}}$, and τ_c^{MB} are computed geometrically as $\tau^{\mathrm{L}} = r_{\mathrm{L}}/c_0$, $\tau_c^{\mathrm{SB}} = (r_c^{\mathrm{S_T}} + r_c^{\mathrm{S_R}})/c_0$, and $\tau_c^{\mathrm{MB}} = (r_c^{\mathrm{M_T}} + r_c^{\mathrm{M_R}})/c_0 + \tau_{\mathrm{VL}}$, respectively, with c_0 denoting the speed of light and τ_{VL} the delay of the virtual link. Here, τ_{VL} is randomly generated

according to the uniform distribution over $(\tau^{\mathrm{L}}, \tau_{\max}]$, where $\tau_{\max}$ is the maximum delay of the virtual link [24].

As there are I_c rays in the link A_p^T–$\mathrm{C}_c^{\mathrm{S}}$–$A_q^R$ and $M_c \times N_c$ rays in the link A_p^T–$\mathrm{C}_c^{\mathrm{M_T}}$–$\mathrm{C}_c^{\mathrm{M_R}}$–$A_q^R$, the LOS, SBC, and MBC components of the CIR are modeled as

$$h_{qp}^{\mathrm{L}}(t) = \sqrt{P_{qp}^{\mathrm{L}}(t)} e^{jk_0 D_{qp}^{\mathrm{L}}(t)} \tag{7}$$

$$h_{qp,c}^{\mathrm{SB}}(t) = \sqrt{P_{qp,c}^{\mathrm{SB}}(t)} \lim_{I_c \to \infty} \sum_{i=1}^{I_c} a_{c,i} e^{-j(k_0 D_{qp,c,i}^{\mathrm{SB}}(t) - \Theta_{c,i}^{\mathrm{SB}})} \tag{8}$$

$$h_{qp,c}^{\mathrm{MB}}(t) = \sqrt{P_{qp,c}^{\mathrm{MB}}(t)} \times \lim_{\substack{M_c \to \infty \\ N_c \to \infty}} \sum_{\substack{m=1 \\ n=1}}^{M_c, N_c} a_{c,mn} e^{-j(k_0 D_{qp,c,mn}^{\mathrm{MB}}(t) - \Theta_{c,mn}^{\mathrm{MB}})} \tag{9}$$

with $j = \sqrt{-1}$ and $k_0 = 2\pi/\lambda$. The terms $\Theta_{c,i}^{\mathrm{SB}}$ and $\Theta_{c,mn}^{\mathrm{MB}}$ are independent and identically distributed (i.i.d.) random variables uniformly distributed over $(0, 2\pi]$ that model the phase shift produced by the scatterers. The amplitudes of the rays $a_{c,i}$ and $a_{c,mn}$ are constrained to $\mathbb{E}[a_{c,i}^2] = 1/I_c$ and $\mathbb{E}[a_{c,nm}^2] = 1/N_c M_c$ with $\mathbb{E}[\cdot]$ denoting the expectation operator. The processes $P_{qp}^{\mathrm{L}}(t)$, $P_{qp,c}^{\mathrm{SB}}(t)$, and $P_{qp,c}^{\mathrm{MB}}(t)$ are the array- and time-dependent local average powers associated to the LOS, SBCs, and MBCs paths, respectively (see Section II-C). The distance traveled by the signal from A_p^{T} to A_q^{R} via $\mathrm{C}_{c,i}^{\mathrm{S}}$ is $D_{qp,c,i}^{\mathrm{SB}}(t) = D_{p,c,i}^{\mathrm{S_T}}(t) + D_{q,c,i}^{\mathrm{S_R}}(t)$, where

$$D_{p,c,i}^{\mathrm{S_T}}(t) = \Big[(r_c^{\mathrm{S_T}})^2 + (v_c^{\mathrm{S_T}} t)^2 + \delta_p^2 + 2r_c^{\mathrm{S_T}} v_c^{\mathrm{S_T}} t \cos\psi_{1,c,i}^{\mathrm{S_T}} - 2r_c^{\mathrm{S_T}} \delta_p \cos\psi_{2,c,i}^{\mathrm{S_T}} - 2\delta_p v_c^{\mathrm{S_T}} t \cos\psi_{3,c}^{\mathrm{S_T}}\Big]^{1/2} \tag{10}$$

and the terms $\cos\psi_{1,c,i}^{\mathrm{S_T}}$, $\cos\psi_{2,c,i}^{\mathrm{S_T}}$, and $\cos\psi_{3,c}^{\mathrm{S_T}}$ are given by

$$\cos\psi_{1,c,i}^{\mathrm{S_T}} = \sin\theta_{c,i}^{\mathrm{S_T}} \sin\zeta_c^{\mathrm{S_T}} \cos(\phi_{c,i}^{\mathrm{S_T}} - \xi_c^{\mathrm{S_T}}) + \cos\theta_{c,i}^{\mathrm{S_T}} \cos\zeta_c^{\mathrm{S_T}} \tag{11}$$

$$\cos\psi_{2,c,i}^{\mathrm{S_T}} = \sin\theta_{c,i}^{\mathrm{S_T}} \sin\beta^{\mathrm{T}} \cos(\phi_{c,i}^{\mathrm{S_T}} - \alpha^{\mathrm{T}}) + \cos\theta_{c,i}^{\mathrm{S_T}} \cos\beta^{\mathrm{T}} \tag{12}$$

$$\cos\psi_{3,c}^{\mathrm{S_T}} = \sin\zeta_c^{\mathrm{S_T}} \sin\beta^{\mathrm{T}} \cos(\xi_c^{\mathrm{S_T}} - \alpha^{\mathrm{T}}) + \cos\zeta_c^{\mathrm{S_T}} \cos\beta^{\mathrm{T}}. \tag{13}$$

The receive-side distance $D_{q,c,i}^{\mathrm{S_R}}(t)$ can be analogously computed by substituting T by R and p by q in (10)–(13). The vector $\vec{C}_{c,i}^{\mathrm{S_R}}(t)$ is related to $\vec{C}_c^{\mathrm{S_T}}(t)$ as $\vec{C}_{c,i}^{\mathrm{S_R}}(t) = \vec{C}_{c,i}^{\mathrm{S_T}}(t) - \vec{R}(t) = \vec{C}_{c,i}^{\mathrm{S_T}}(0) - \vec{R}(0) + (\vec{v}_c^{\mathrm{S_T}} - \vec{v}_{\mathrm{R}})t = \vec{C}_{c,i}^{\mathrm{S_R}}(0) + \vec{v}_c^{\mathrm{S_R}} t$. Hence, the spherical coordinates of $\vec{C}_c^{\mathrm{S_R}}(0)$ are

$$\theta_{c,i}^{\mathrm{S_R}} = \cos^{-1}\left(\frac{r_c^{\mathrm{S_T}} \cos\theta_{c,i}^{\mathrm{S_T}} - r_{\mathrm{L}} \cos\theta^{\mathrm{L}}}{r_c^{\mathrm{S_R}}}\right) \tag{14}$$

$$\phi_{c,i}^{\mathrm{S_R}} = \tan^{-1}\left(\frac{r_c^{\mathrm{S_T}} \sin\theta_{c,i}^{\mathrm{S_T}} \sin\phi_{c,i}^{\mathrm{S_T}} - r_{\mathrm{L}} \sin\theta^{\mathrm{L}} \sin\phi^{\mathrm{L}}}{r_c^{\mathrm{S_T}} \sin\theta_{c,i}^{\mathrm{S_T}} \cos\phi_{c,i}^{\mathrm{S_T}} - r_{\mathrm{L}} \sin\theta^{\mathrm{L}} \cos\phi^{\mathrm{L}}}\right) \tag{15}$$

where the distance $r_c^{\mathrm{S_R}}$ from the center of the receiving array to the SBC can be obtained as

$$r_c^{\mathrm{S_R}} = \left(r_{\mathrm{L}}^2 + (r_c^{\mathrm{S_T}})^2 - 2r_{\mathrm{L}} r_c^{\mathrm{S_T}} \cos\psi_{4,c,i}\right)^{1/2} \tag{16}$$

with

$$\cos\psi_{4,c,i} = \sin\theta_{c,i}^{\mathrm{S_T}} \sin\theta^{\mathrm{L}} \cos(\phi_{c,i}^{\mathrm{S_T}} - \phi^{\mathrm{L}}) + \cos\theta_{c,i}^{\mathrm{S_T}} \cos\theta^{\mathrm{L}}. \tag{17}$$

The distance traveled by the the rays from A_p^{T} to A_q^{R} via the cth MBC is $D_{qp,c,mn}^{\mathrm{MB}}(t) = D_{p,c,m}^{\mathrm{M_T}}(t) + D_{q,c,n}^{\mathrm{M_R}}(t) + c_0 \cdot \tau_{\mathrm{VL}}$, where

$$D_{p,c,m}^{\mathrm{M_T}}(t) = \Big[(r_c^{\mathrm{M_T}})^2 + (v_c^{\mathrm{M_T}} t)^2 + \delta_p^2 + 2r_c^{\mathrm{M_T}} v_c^{\mathrm{M_T}} t \cos\psi_{1,c,m}^{\mathrm{M_T}} - 2r_c^{\mathrm{M_T}} \delta_p \cos\psi_{2,c,m}^{\mathrm{M_T}} - 2\delta_p v_c^{\mathrm{M_T}} t \cos\psi_{3,c}^{\mathrm{M_T}}\Big]^{1/2} \tag{18}$$

where $\cos\psi_{1,c,m}^{\mathrm{M_T}}$, $\cos\psi_{2,c,m}^{\mathrm{M_T}}$, and $\cos\psi_{c,3}^{\mathrm{M_T}}$ are computed analogously to (11)–(13) and hence they are omitted. The receive-side distance $D_{q,c,n}^{\mathrm{M_R}}(t)$ can be computed by substituting T by R, p by q, and m by n in (18). Unlike SBCs, there is no relationship between the transmit- and receive-side representations of MBCs.

The distance associated to the LOS path from A_p^{T} to A_q^{R} is

$$D_{qp}^{\mathrm{L}}(t) = \big[r_{\mathrm{L}}^2 + (v_{\mathrm{R}} t)^2 + \delta_q^2 + \delta_p^2 + 2r_{\mathrm{L}} v_{\mathrm{R}} t \cos\psi_1^{\mathrm{L}} + 2r_{\mathrm{L}}\delta_q \cos\psi_2^{\mathrm{L}} - 2r_{\mathrm{L}}\delta_p \cos\psi_3^{\mathrm{L}} + 2\delta_q v_{\mathrm{R}} t \cos\psi_4^{\mathrm{L}} - 2\delta_p v_{\mathrm{R}} t \cos\psi_5^{\mathrm{L}} - 2\delta_q\delta_p \cos\psi_6^{\mathrm{L}}\big]^{1/2} \tag{19}$$

where the terms $\cos\psi_i^{\mathrm{L}}$ for $i = 1, 2, \ldots, 6$ are given by

$$\cos\psi_1^{\mathrm{L}} = \sin\theta^{\mathrm{R}} \sin\zeta^{\mathrm{R}} \cos(\phi^{\mathrm{R}} - \xi^{\mathrm{R}}) + \cos\theta^{\mathrm{R}} \cos\zeta^{\mathrm{R}} \tag{20}$$

$$\cos\psi_2^{\mathrm{L}} = \sin\theta^{\mathrm{R}} \sin\beta^{\mathrm{R}} \cos(\phi^{\mathrm{R}} - \alpha^{\mathrm{R}}) + \cos\theta^{\mathrm{R}} \cos\beta^{\mathrm{R}} \tag{21}$$

$$\cos\psi_3^{\mathrm{L}} = \sin\theta^{\mathrm{R}} \sin\beta^{\mathrm{T}} \cos(\phi^{\mathrm{R}} - \alpha^{\mathrm{T}}) + \cos\theta^{\mathrm{R}} \cos\beta^{\mathrm{T}} \tag{22}$$

$$\cos\psi_4^{\mathrm{L}} = \sin\zeta^{\mathrm{R}} \sin\beta^{\mathrm{R}} \cos(\xi^{\mathrm{R}} - \alpha^{\mathrm{R}}) + \cos\zeta^{\mathrm{R}} \cos\beta^{\mathrm{R}} \tag{23}$$

$$\cos\psi_5^{\mathrm{L}} = \sin\zeta^{\mathrm{R}} \sin\beta^{\mathrm{T}} \cos(\xi^{\mathrm{R}} - \alpha^{\mathrm{T}}) + \cos\zeta^{\mathrm{R}} \cos\beta^{\mathrm{T}} \tag{24}$$

$$\cos\psi_6^{\mathrm{L}} = \sin\beta^{\mathrm{T}} \sin\beta^{\mathrm{R}} \cos(\alpha^{\mathrm{T}} - \alpha^{\mathrm{R}}) + \cos\beta^{\mathrm{T}} \cos\beta^{\mathrm{R}}. \tag{25}$$

B. Second-Order Approximation to the Wavefronts: Spatial-Temporal Parabolic Wavefronts

Equations (10), (18), and (19) enable to model near-field effects and non-stationary properties of the channel in arbitrary situations. However, second-order approximations to these expressions can capture the non-stationary properties of the CIR for small angular drifts and reduce the computational complexity. The second-order Taylor series expansion of the distance $D_{p,c,i}^{\mathrm{S_T}}(t)$ in (10) with respect to the ratios $\delta_p/r_c^{\mathrm{S_T}}$ and $v_c^{\mathrm{S_T}} t/r_c^{\mathrm{S_T}}$ when $\delta_p/r_c^{\mathrm{S_T}} < 1$ and $v_c^{\mathrm{S_T}} t/r_c^{\mathrm{S_T}} < 1$ is

$$D_{p,c,i}^{\mathrm{S_T}}(t) \approx \overbrace{r_c^{\mathrm{S_T}} + v_c^{\mathrm{S_T}} t \cos\psi_{1,c,i}^{\mathrm{S_T}} - \delta_p \cos\psi_{2,c,i}^{\mathrm{S_T}}}^{\text{Plane-wavefront approximation}} \overbrace{+ \frac{(v_c^{\mathrm{S_T}} t)^2}{2r_c^{\mathrm{S_T}}} \sin^2\psi_{1,c,i}^{\mathrm{S_T}} + \frac{\delta_p^2}{2r_c^{\mathrm{S_T}}} \sin^2\psi_{2,c,i}^{\mathrm{S_T}} + \frac{v_c^{\mathrm{S_T}} t \delta_p}{r_c^{\mathrm{S_T}}} Q(\psi_{1,c,i}^{\mathrm{S_T}}, \psi_{2,c,i}^{\mathrm{S_T}}, \psi_{3,c}^{\mathrm{S_T}})}^{\text{Parabolic-wavefront approximation}} \tag{26}$$

where we defined $Q(\psi_i, \psi_j, \psi_k) = \cos\psi_i \cos\psi_j - \cos\psi_k$. Analogously, the distances $D_{q,c,i}^{\mathrm{S_R}}(t)$, $D_{p,c,m}^{\mathrm{M_T}}(t)$, and $D_{q,c,n}^{\mathrm{M_R}}(t)$

can be approximated by substituting $\{S_T, i, p\}$ by $\{S_R, i, q\}$, $\{M_T, n, p\}$, and $\{M_R, m, q\}$ in (26), respectively. The distance of the LOS path $D^L_{qp}(t)$ can be approximated as

$$D^L_{qp}(t) \approx \overbrace{r_L + v_R t\cos\psi^L_1 + \delta_q\cos\psi^L_2 - \delta_p\cos\psi^L_3}^{\text{Plane-wavefront approximation}} + \overbrace{\frac{(v_R t)^2}{2r_L}\sin^2\psi^L_1 + \frac{\delta_q^2}{2r_L}\sin^2\psi^L_2 + \frac{\delta_p^2}{2r_L}\sin^2\psi^L_3}^{\text{Parabolic-wavefront approximation}} - \frac{\delta_q v_R t}{r_L}Q(\psi^L_1,\psi^L_2,\psi^L_4) + \frac{\delta_p v_R t}{r_L}Q(\psi^L_1,\psi^L_3,\psi^L_5) + \frac{\delta_q\delta_p}{r_L}Q(\psi^L_2,\psi^L_3,\psi^L_6). \quad (27)$$

Unlike the first-order terms in (26) and (27), labeled as *plane-wavefront approximation*, the second-order terms and cross-products, labeled as *parabolic-wavefront approximation*, depend on the distances to the cluster $r_c^{S_T}$ and between the arrays r_L, respectively. Subsequently, it will be shown that the second-order terms cause the non-stationarity of the CIR in time and space. In addition, the time-array cross-products, e.g., $v_c^{S_T} t\cdot\delta_p$, lead to a dependence of the spatial CCF (S-CCF) and temporal autocorrelation function (ACF) with respect to time and space, respectively. Note that the second-order terms are reduced to zero for small arrays and short periods of time, i.e., $\delta_p/r_L \ll 1$, $\delta_p/r_c^{S_T} \ll 1$, $v_R t/r_L \ll 1$, and $v_c^{S_T} t/r_c^{S_T} \ll 1$. In these conditions, only the first-order terms in (26) and (27) remain as in conventional MIMO channel models [15]–[19].

On one hand, it is usually considered that the accuracy of the approximation obtained through the second-order expansion of (10) is excellent when the ratios $\delta_p/r_L, \delta_p/r_c^{S_T}, v_R t/r_L$, and $v_c^{S_T} t/r_c^{S_T}$ are lower than 0.1. Using this criterion, the parabolic wavefront approximation in (26) can be considered very accurate when the distance from the center of the array to any cluster is at least 5 times the length of the ULA. Nonetheless, we will show in Section V that very accurate results of the statistical properties of the channel model can be obtained using the parabolic wavefront under less conservative conditions. On the other hand, the reduction of the computational complexity associated to the parabolic wavefront compared to that of the spherical wavefront is obtained from the simplification of the exact distance in (10) to the second-order polynomial in (26). Firstly, with the same number of terms in (10) and (26), the second-order approximation does not require the repetitive computation of the square root function in (10) for every AoA in every cluster at any time instant and antenna element of the receive array. Secondly, efficient quadratic-phase rotation algorithms, which are analogous to the efficient linear-phase rotation algorithms used in the case of the plane wavefront [21], can be employed to compute the phase associated to the parabolic wavefront.

C. Cluster and LOS Evolution: Shadowing and Reappearance

Variations of the average received power in time and over the array are caused by *(re)appearance* and *shadowing* of both LOS and cluster components, which are modeled here by *Markov two-state* and *lognormal shadowing* processes, respectively. As in [28], in this paper the WINNER+ [16] and COST 2100 [18] models are used as references for the development of the cluster evolution processes. In [16] and [18], the average power associated to the cth cluster is modeled as

$$P_c = \exp\left[-\tau_c\frac{r_\tau - 1}{r_\tau\sigma_{\tau,c}}\right]\cdot 10^{-\frac{\nu_c}{10}} \quad (28)$$

where τ_c is the delay of the signal scattered by the cth cluster, $\sigma_{\tau,c}$ is the delay spread (DS) of the channel, and r_τ is the ratio of the standard deviation of the delays to the root mean square (RMS) DS. The parameter ν_c is a zero-mean Gaussian random variable used to model a shadowing randomization effect on each cluster for each stationary simulation drop or segment [16], [18]. Since the cluster-level evolution processes for LOS, SBCs, and MBCs are analogous, only the SBC case will be considered in the following. Only when it is necessary, the differences between SBCs and MBCs will be pointed out. In this model, we propose the following modification

$$P^{SB}_{qp,c}(t) = \exp\left[-\tau_c\frac{r_\tau - 1}{r_\tau\sigma_{\tau,c}}\right]\cdot\gamma^{SB}_{qp,c}(t)\cdot\Pi^{SB}_{qp,c}(t) \quad (29)$$

where the shadowing randomization factor $10^{-\frac{\nu_c}{10}}$ in (28) is superseded by the product of the processes $\gamma^{SB}_{qp,c}(t)$ and $\Pi^{SB}_{qp,c}(t)$. First, cluster (re)appearance (visibility) is modeled by a two-state Markov process $\Pi^{SB}_{qp,c}(t)$. Second, smooth variations of the clusters average power in time domain and over both arrays are modeled by a lognormal process $\gamma^{SB}_{qp,c}(t)$. Analogously, transitions between LOS and NLOS states and smooth power variations of the LOS component are modeled by the processes $\Pi^L_{qp}(t)$ and $\gamma^L_{qp}(t)$, respectively. Thus, the local average power of the LOS component in (7) is $P^L_{qp}(t) = \gamma^L_{qp}(t)\cdot\Pi^L_{qp}(t)$.

1) Spatial-Temporal LOS/Cluster Reappearance: The product of the three two-state Markov processes $\Pi_c^{S_T}(\delta_p)$, $\Pi_c^{S_R}(\delta_q)$, and $\Pi_c^{SB}(t)$ models cluster (re)appearance over the transmit- and receive-arrays and in time, respectively. As every cluster may only be visible over certain array and time intervals, these processes take value (0)1 if the cluster is (in)visible over the corresponding dimensions. The product of the processes is used because a cluster is visible only if it is visible from both sides of the communication link at the same time. Similarly to [23], [24], and [30], the size of the invisibility and VRs of a cluster is modeled by exponential i.i.d. random variables with intensities λ_I and λ_V, respectively. For the spatial process $\Pi_c^{S_T}(\delta_p)$ the transition matrix is [31]

$$\mathbf{T}_c(\delta_p) = \begin{pmatrix} P^{S_T}_{I,c} + P^{S_T}_{V,c}e^{-\lambda^{S_T}_{T,c}\delta_p} & P^{S_T}_{V,c} - P^{S_T}_{V,c}e^{-\lambda^{S_T}_{T,c}\delta_p} \\ P^{S_T}_{I,c} - P^{S_T}_{I,c}e^{-\lambda^{S_T}_{T,c}\delta_p} & P^{S_T}_{V,c} + P^{S_T}_{I,c}e^{-\lambda^{S_T}_{T,c}\delta_p} \end{pmatrix} \quad (30)$$

where $\lambda^{S_T}_{T,c} = \lambda^{S_T}_{V,c} + \lambda^{S_T}_{I,c}$. The entries in the transition matrix in (30) represent the probability of transition between visibility and invisibility regions of a cluster. The probabilities that a cluster is visible or invisible at any position along the array are $P^{S_T}_{V,c} = \lambda^{S_T}_{V,c}/\lambda^{S_T}_{T,c}$ or $P^{S_T}_{I,c} = \lambda^{S_T}_{I,c}/\lambda^{S_T}_{T,c}$, respectively. For the temporal process $\Pi_c^{SB}(t)$, the transition matrix must be modified by substituting δ_p by the channel fluctuation $q(t)$, which can be expressed as $q(t) = (v_c^{S_T} + v_c^{S_R})t$ assuming

constant cluster and Rx speeds [30]. Note that unlike the models in [23], [24], and [30], the transition rates $\lambda_{V,c}^{\mathrm{S_T}}$ and $\lambda_{I,c}^{\mathrm{S_T}}$ might be different for every cluster and dependent of the characteristics of the environment, hence resulting in a more flexible model. The total spatial-temporal (re)appearance process for SBCs is given by

$$\Pi_{qp,c}^{\mathrm{SB}}(t) = \Pi_c^{\mathrm{S_T}}(\delta_p) \cdot \Pi_c^{\mathrm{S_R}}(\delta_q) \cdot \Pi_c^{\mathrm{SB}}(t). \tag{31}$$

Finally, it is important to highlight that unlike previous models where clusters can only (dis)appear, the reappearance process proposed here can model clusters that keep their properties while they are occluded before becoming visible again. This results in a higher spatial consistency of the channel and reduces the total number of clusters generated per simulation.

2) Spatial-Temporal LOS/Cluster Shadowing: Applying the concept of spatial shadowing processes described in [32]–[34], the spatial-temporal shadowing process $\gamma_{qp,c}^{\mathrm{SB}}(t)$ can be obtained as the product of three lognormal processes: two spatial processes evaluated at the positions of every antenna element of the transmit/receive array and a temporal process to account for smooth power variations in time domain. Thus, the process $\gamma_{qp,c}^{\mathrm{SB}}(t)$ can be expressed as

$$\gamma_{qp,c}^{\mathrm{SB}}(t) = 10^{\left(m_c^{\mathrm{SB}} + \sigma_c^{\mathrm{SB}} \nu_c^{\mathrm{SB}}(t) + \sigma_c^{\mathrm{S_T}} \nu_c^{\mathrm{S_T}}(\delta_p) + \sigma_c^{\mathrm{S_R}} \nu_c^{\mathrm{S_R}}(\delta_q)\right)/10} \tag{32}$$

where the terms $\nu_c^{\mathrm{S_T}}(\delta_p)$, $\nu_c^{\mathrm{S_R}}(\delta_q)$, and $\nu_c^{\mathrm{SB}}(t)$ are three independent real-valued zero-mean Gaussian WSS processes with unit variance. The parameters $\sigma_c^{\mathrm{S_T}}$, $\sigma_c^{\mathrm{S_R}}$, and σ_c^{SB} are the *shadow standard deviations* of the cluster's power and m_c^{SB} is called the *area mean*. Since they are zero-mean independent Gaussian processes, the resulting sum $\sigma_c^{S_T}\nu_c^{\mathrm{S_T}}(\delta_p) + \sigma_c^{S_R}\nu_c^{\mathrm{S_R}}(\delta_q) + \sigma_c^{\mathrm{SB}}\nu_c^{\mathrm{SB}}(t)$ is also a zero-mean Gaussian process whose standard deviation is $\sigma_c^e = [(\sigma_c^{\mathrm{S_T}})^2 + (\sigma_c^{\mathrm{S_R}})^2 + (\sigma_c^{\mathrm{SB}})^2]^{1/2}$. As indicated in (32), the standard deviations and area mean can be different for every cluster and dependent of the characteristics of the environment. Usually, the parameter m_c^{SB} depends on the distance between the arrays and the cluster, frequency, and other parameters of the path-loss model applied [32]. As we will show, the parameter σ_c^e controls the amplitude of the power variations over the array and in time.

The theoretical model of the process $\nu_c^{\mathrm{S_T}}(\delta_p)$ is an infinite sum-of-sinusoids (SoS) [33], i.e.,

$$\nu_c^{\mathrm{S_T}}(\delta_p) = \lim_{K_c^{\mathrm{S_T}} \to \infty} \sum_{n=1}^{K_c^{\mathrm{S_T}}} b_{c,n}^{\mathrm{S_T}} \cos\left(2\pi s_{c,n}^{\mathrm{S_T}} \delta_p + \Theta_{c,n}^{\mathrm{S_T}}\right) \tag{33}$$

where $K_c^{\mathrm{S_T}}$, $s_{c,n}^{\mathrm{S_T}}$, $b_{c,n}^{\mathrm{S_T}}$, and $\Theta_{c,n}^{\mathrm{S_T}}$ denote the number of sinusoids, the spatial frequency, amplitude, and initial phase of each sinusoid, respectively. The phases $\Theta_{c,n}^{\mathrm{S_T}}$ are i.i.d. random variables uniformly distributed over $[0, 2\pi)$ and the amplitudes $b_{c,n}^{\mathrm{S_T}}$ are subject to the condition $\mathbb{E}[(b_{c,n}^{\mathrm{S_T}})^2] = 1/K_c^{\mathrm{S_T}}$. Analogously, the temporal lognormal process $\nu_c^{\mathrm{SB}}(t)$ is given by

$$\nu_c^{\mathrm{SB}}(t) = \lim_{K_c^{\mathrm{SB}} \to \infty} \sum_{n=1}^{K_c^{\mathrm{SB}}} b_{c,n}^{\mathrm{SB}} \cos\left(2\pi f_{c,n}^{\mathrm{SB}} t + \theta_{c,n}^{\mathrm{SB}}\right) \tag{34}$$

where $f_{c,n}^{\mathrm{SB}}$ denotes the temporal frequency of the nth sinusoid and the rest of the parameters have an analogous meaning to those of the spatial processes in (33).

III. Statistical Properties of the Theoretical Channel Model

In this section, key statistical properties of the model, e.g., the ST-CCF and Doppler frequency shifts, considering the parabolic wavefront, cluster (re)appearance, and cluster shadowing will be derived.

A. Spatial-Temporal Cross-Correlation Function (ST-CCF)

The ST-CCF, defined as $\mathbb{E}[h_{qp}(t,\tau)h_{q'p'}^*(t+\Delta t,\tau)]$, can be separated into three terms as

$$\begin{aligned}\rho_{qp}&(\delta_{\mathrm{T}}, \delta_{\mathrm{R}}, \Delta t, t) \\ &= \rho_{qp}^{\mathrm{L}}(\delta_{\mathrm{T}}, \delta_{\mathrm{R}}, \Delta t, t) + \sum_{c=1}^{C_{\mathrm{S}}} \rho_{qp,c}^{\mathrm{SB}}(\delta_{\mathrm{T}}, \delta_{\mathrm{R}}, \Delta t, t) \\ &\quad + \sum_{c=1}^{C_{\mathrm{M}}} \rho_{qp,c}^{\mathrm{MB}}(\delta_{\mathrm{T}}, \delta_{\mathrm{R}}, \Delta t, t)\end{aligned} \tag{35}$$

where uncorrelated scattering (US) in the delay domain was assumed. Due to the independence of the large-scale and small-scale fading processes, every ST-CCF can be expressed as the product of a large-scale and small-scale ST-CCF, e.g., $\rho_{qp,c}^{\mathrm{SB}}(\delta_{\mathrm{T}}, \delta_{\mathrm{R}}, \Delta t, t) = \rho_{\mathrm{LS},qp,c}^{\mathrm{SB}}(\delta_{\mathrm{T}}, \delta_{\mathrm{R}}, \Delta t) \cdot \rho_{\mathrm{SS},qp,c}^{\mathrm{SB}}(\delta_{\mathrm{T}}, \delta_{\mathrm{R}}, \Delta t, t)$. Note that the large-scale ST-CCF does not depend on absolute time t since, as it will be demonstrated, the (re)appearance and shadowing processes are WSS. Next, these correlation functions are derived and analyzed.

1) Small-Scale ST-CCF: The small-scale ST-CCFs of the LOS, SBCs, and MBCs are

$$\rho_{\mathrm{SS},qp}^{\mathrm{L}}(\delta_{\mathrm{T}}, \delta_{\mathrm{R}}, \Delta t, t) = e^{-jk_0 \Delta_{qp}^{\mathrm{L}}(\delta_{\mathrm{T}}, \delta_{\mathrm{R}}, \Delta t, t)} \tag{36}$$

$$\begin{aligned}\rho_{\mathrm{SS},qp,c}^{\mathrm{SB}}&(\delta_{\mathrm{T}}, \delta_{\mathrm{R}}, \Delta t, t) \\ &= \lim_{I_c \to \infty} \sum_{i=1}^{I_c} \mathbb{E}\left[a_{c,i}^2 e^{-jk_0 \Delta_{qp,c,i}^{\mathrm{SB}}(\delta_{\mathrm{T}}, \delta_{\mathrm{R}}, \Delta t, t)}\right]\end{aligned} \tag{37}$$

$$\begin{aligned}\rho_{\mathrm{SS},qp,c}^{\mathrm{MB}}&(\delta_{\mathrm{T}}, \delta_{\mathrm{R}}, \Delta t, t) \\ &= \lim_{\substack{M_c \to \infty \\ N_c \to \infty}} \sum_{\substack{m=1 \\ n=1}}^{M_c, N_c} \mathbb{E}\left[a_{c,mn}^2 e^{-jk_0 \Delta_{qp,c,nm}^{\mathrm{MB}}(\delta_{\mathrm{T}}, \delta_{\mathrm{R}}, \Delta t, t)}\right]\end{aligned} \tag{38}$$

where the distance differences are $\Delta_{qp}^{\mathrm{L}}(\delta_{\mathrm{T}}, \delta_{\mathrm{R}}, \Delta t, t) = D_{qp}^{\mathrm{L}}(t) - D_{q'p'}^{\mathrm{L}}(t + \Delta t)$, $\Delta_{qp,c,i}^{\mathrm{SB}}(\delta_{\mathrm{T}}, \delta_{\mathrm{R}}, \Delta t, t) = D_{qp,c,i}^{\mathrm{SB}}(t) - D_{q'p',c,i}^{\mathrm{SB}}(t + \Delta t)$, and $\Delta_{qp,c,mn}^{\mathrm{MB}}(\delta_{\mathrm{T}}, \delta_{\mathrm{R}}, \Delta t, t) = D_{qp,c,mn}^{\mathrm{MB}}(t) - D_{q'p',c,mn}^{\mathrm{MB}}(t + \Delta t)$. Thus, using the second-order approximations in (26) and (27), $\Delta_{qp}^{\mathrm{L}}(\delta_{\mathrm{T}}, \delta_{\mathrm{R}}, \Delta t, t)$ is computed as indicated in (39), where $\Delta_{pp'} = \delta_{\mathrm{T}}(p - p')$ and $\Delta_{qq'} = \delta_{\mathrm{R}}(q - q')$.

For the case of SBCs and MBCs in (37) and (38), it can be seen that the distance differences can be expressed as $\Delta_{qp,c,i}^{\mathrm{SB}}(\delta_{\mathrm{T}}, \delta_{\mathrm{R}}, \Delta t, t) = \Delta_{p,c,i}^{\mathrm{S_T}}(\delta_{\mathrm{T}}, \Delta t, t) + \Delta_{q,c,i}^{\mathrm{S_R}}(\delta_{\mathrm{R}}, \Delta t, t)$ for SBCs and $\Delta_{qp,c,mn}^{\mathrm{MB}}(\delta_{\mathrm{T}}, \delta_{\mathrm{R}}, \Delta t, t) = \Delta_{p,c,m}^{\mathrm{M_T}}(\delta_{\mathrm{T}}, \Delta t, t) + \Delta_{q,c,n}^{\mathrm{M_R}}(\delta_{\mathrm{R}}, \Delta t, t)$ for MBCs, where $\Delta_{p,c,i}^{\mathrm{S_T}}(\delta_{\mathrm{T}}, \Delta t, t)$ is

$$\begin{aligned}
&\Delta^{\mathrm{L}}_{qp}(\delta_{\mathrm{T}},\delta_{\mathrm{R}},\Delta t,t)\\
&\approx -v_{\mathrm{R}}\Delta t\cos\psi^{\mathrm{L}}_1-\Delta_{qq'}\cos\psi^{\mathrm{L}}_2+\Delta_{pp'}\cos\psi^{\mathrm{L}}_3-\frac{v^2_{\mathrm{R}}\Delta t(\Delta t+2t)}{2r_{\mathrm{L}}}\sin^2\psi^{\mathrm{L}}_1-\frac{\Delta_{qq'}(\Delta_{qq'}+2\delta_q)}{2r_{\mathrm{L}}}\sin^2\psi^{\mathrm{L}}_2\\
&\quad-\frac{\Delta_{pp'}(\Delta_{pp'}+2\delta_p)}{2r_{\mathrm{L}}}\sin^2\psi^{\mathrm{L}}_3+\frac{v_{\mathrm{R}}t\Delta_{qq'}+v_{\mathrm{R}}\Delta t\delta_{q'}}{r_{\mathrm{L}}}Q(\psi^{\mathrm{L}}_1,\psi^{\mathrm{L}}_2,\psi^{\mathrm{L}}_4)-\frac{v_{\mathrm{R}}t\Delta_{pp'}+v_{\mathrm{R}}\Delta t\delta_{p'}}{r_{\mathrm{L}}}Q(\psi^{\mathrm{L}}_1,\psi^{\mathrm{L}}_3,\psi^{\mathrm{L}}_5)\\
&\quad-\frac{(N_{\mathrm{R}}+1)\delta_{\mathrm{R}}\Delta_{pp'}+(N_{\mathrm{T}}+1)\delta_{\mathrm{T}}\Delta_{qq'}-(qp-q'p')\delta_{\mathrm{T}}\delta_{\mathrm{R}}}{r_{\mathrm{L}}}Q(\psi^{\mathrm{L}}_2,\psi^{\mathrm{L}}_3,\psi^{\mathrm{L}}_6).
\end{aligned}\tag{39}$$

$$\begin{aligned}
\Delta^{\mathrm{S_T}}_{p,c,i}(\delta_{\mathrm{T}},\Delta t,t)\approx&-v^{\mathrm{S_T}}_c\Delta t\cos\psi^{\mathrm{S_T}}_{1,c,i}+\Delta_{pp'}\cos\psi^{\mathrm{S_T}}_{2,c,i}-\frac{(v^{\mathrm{S_T}}_c)^2\Delta t(\Delta t+2t)}{2r^{\mathrm{S_T}}_c}\sin^2\psi^{\mathrm{S_T}}_{1,c,i}\\
&-\frac{\Delta_{pp'}(\Delta_{pp'}+2\delta_p)}{2r^{\mathrm{S_T}}_c}\sin^2\psi^{\mathrm{S_T}}_{2,c,i}-\frac{1}{r^{\mathrm{S_T}}_c}\left(v^{\mathrm{S_T}}_c t\Delta_{pp'}+v^{\mathrm{S_T}}_c\Delta t\delta_{p'}\right)Q(\psi^{\mathrm{S_T}}_{1,c,i},\psi^{\mathrm{S_T}}_{2,c,i},\psi^{\mathrm{S_T}}_{3,c})
\end{aligned}\tag{40}$$

obtained as indicated in (40). The difference $\Delta^{\mathrm{S_R}}_{q,c,i}(\delta_{\mathrm{R}},\Delta t,t)$ can be analogously computed by substituting $\mathrm{S_T}$ by $\mathrm{S_R}$ and p by q in (40). The terms $\Delta^{\mathrm{M_T}}_{p,c,m}(\delta_{\mathrm{T}},\Delta t,t)$ and $\Delta^{\mathrm{M_R}}_{q,c,n}(\delta_{\mathrm{R}},\Delta t,t)$ can be computed analogously and they are omitted here for brevity.

In the limit $I_c\to\infty$, the ST-CCF of the SBC in (37) can be computed as [33]

$$\begin{aligned}
\rho^{\mathrm{SB}}_{\mathrm{SS},qp,c}(\delta_{\mathrm{T}},\delta_{\mathrm{R}},\Delta t,t)=&\int_{-\pi}^{\pi}\int_0^{\pi}e^{-jk_0\Delta^{\mathrm{SB}}_{qp,c}(\delta_{\mathrm{T}},\delta_{\mathrm{R}},\Delta t,t)}\\
&\times f^{\mathrm{S_T}}_c(\theta^{\mathrm{S_T}}_c,\phi^{\mathrm{S_T}}_c)\mathrm{d}\theta^{\mathrm{S_T}}_c\mathrm{d}\phi^{\mathrm{S_T}}_c
\end{aligned}\tag{41}$$

where the discrete random variables $\Delta^{\mathrm{SB}}_{qp,c,i}(\delta_{\mathrm{T}},\delta_{\mathrm{R}},\Delta t,t)$, $\phi^{\mathrm{S_T(R)}}_{c,i}$, $\theta^{\mathrm{S_T(R)}}_{c,i}$, $\psi^{\mathrm{S_T(R)}}_{1,c,i}$, and $\psi^{\mathrm{S_T(R)}}_{2,c,i}$ in (37) have been substituted by their continuous versions $\Delta^{\mathrm{SB}}_{qp,c}(\delta_{\mathrm{T}},\delta_{\mathrm{R}},\Delta t,t)$, $\phi^{\mathrm{S_T(R)}}_c$, $\theta^{\mathrm{S_T(R)}}_c$, $\psi^{\mathrm{S_T(R)}}_{1,c}$, and $\psi^{\mathrm{S_T(R)}}_{2,c}$, respectively. The function $f^{\mathrm{S_T}}_c(\theta^{\mathrm{S_T}}_c,\phi^{\mathrm{S_T}}_c)$ denotes the joint probability density function (pdf) of the elevation AoDs (EAoDs) and azimuth AoDs (AAoDs) of $\mathrm{C^S_c}$. The elevation AoAs (EAoAs) and azimuth AoAs (AAoAs) implicit in (41) are a function of the AoDs as indicated in (14) and (15).

Due to the angular independence of the transmit- and receive-side MBCs, this MBC contribution to the ST-CCF in (38) admits a Kronecker form as the product of the transmit-side and receive-side ST-CCFs, i.e., $\rho^{\mathrm{MB}}_{\mathrm{SS},qp,c}(\delta_{\mathrm{T}},\delta_{\mathrm{R}},\Delta t,t)=\rho^{\mathrm{M_T}}_{\mathrm{SS},pp',c}(\delta_{\mathrm{T}},\Delta t,t)\cdot\rho^{\mathrm{M_R}}_{\mathrm{SS},qq',c}(\delta_{\mathrm{R}},\Delta t,t)$. In the limit as $M_c,N_c\to\infty$, the transmit-side and receive-side ST-CCF are

$$\begin{aligned}
\rho^{\mathrm{M_T}}_{\mathrm{SS},pp',c}(\delta_{\mathrm{T}},\Delta t,t)=&\int_{-\pi}^{\pi}\int_0^{\pi}e^{-jk_0\Delta^{\mathrm{M_T}}_{pp',c}(\delta_{\mathrm{T}}\Delta t,t)}\\
&\times f^{\mathrm{M_T}}_c(\theta^{\mathrm{M_T}}_c,\phi^{\mathrm{M_T}}_c)\mathrm{d}\theta^{\mathrm{M_T}}_c\mathrm{d}\phi^{\mathrm{M_T}}_c
\end{aligned}\tag{42}$$

$$\begin{aligned}
\rho^{\mathrm{M_R}}_{\mathrm{SS},qq',c}(\delta_{\mathrm{R}},\Delta t,t)=&\int_{-\pi}^{\pi}\int_0^{\pi}e^{-jk_0\Delta^{\mathrm{M_R}}_{qq',c}(\delta_{\mathrm{R}},\Delta t,t)}\\
&\times f^{\mathrm{M_R}}_c(\theta^{\mathrm{M_R}}_c,\phi^{\mathrm{M_R}}_c)\mathrm{d}\theta^{\mathrm{M_R}}_c\mathrm{d}\phi^{\mathrm{M_R}}_c
\end{aligned}\tag{43}$$

where the discrete random variables $\phi^{\mathrm{M_T}}_{c,m}$, $\phi^{\mathrm{M_R}}_{c,n}$, $\theta^{\mathrm{M_T}}_{c,m}$, $\theta^{\mathrm{M_R}}_{c,n}$, $\psi^{\mathrm{M_T}}_{1,c,m}$, $\psi^{\mathrm{M_R}}_{1,c,n}$, $\psi^{\mathrm{M_T}}_{2,c,m}$, $\psi^{\mathrm{M_R}}_{2,c,n}$, and $\Delta^{\mathrm{MB}}_{qp,c,mn}(\delta_{\mathrm{T}},\delta_{\mathrm{R}},\Delta t,t)$ in (38) have been substituted by $\phi^{\mathrm{M_T}}_c$, $\phi^{\mathrm{M_R}}_c$, $\theta^{\mathrm{M_T}}_c$, $\theta^{\mathrm{M_R}}_c$, $\psi^{\mathrm{M_T}}_{1,c}$, $\psi^{\mathrm{M_R}}_{1,c}$, $\psi^{\mathrm{M_T}}_{2,c}$, $\psi^{\mathrm{M_R}}_{2,c}$, and $\Delta^{\mathrm{MB}}_{qp,c}(\delta_{\mathrm{T}},\delta_{\mathrm{R}},\Delta t,t)$, respectively. The function $f^{\mathrm{M_T}}_c(\theta^{\mathrm{M_T}}_c,\phi^{\mathrm{M_T}}_c)$ denotes the joint pdf of the EAoD and AAoD of $\mathrm{C^{M_T}_c}$ and $f^{\mathrm{M_R}}_c(\theta^{\mathrm{M_R}}_c,\phi^{\mathrm{M_R}}_c)$ the joint pdf of the EAoA and AAoA of $\mathrm{C^{M_R}_c}$.

Equations (36)–(43), specially (40), show that the ST-CCF does not only depend on relative time and antenna positions Δt and $\Delta_{pp'}$, but also on absolute time t and antenna position δ_p, demonstrating the non-stationary properties of the CIR in both temporal and spatial (over the array) domains, respectively. The terms dependent of the ratios $v^{\mathrm{S_T}}_c t/r^{\mathrm{S_T}}_c,\delta_p/r^{\mathrm{S_T}}_c$ indicate that the closer the cluster is to the Tx, the more it contributes to the non-stationarity of the CIR. In addition, the cross-products, e.g., $v_{\mathrm{R}}t\cdot\delta_p, v^{\mathrm{S_T}}_c t\cdot\delta_p$, introduce cross-dependencies into the correlation functions with respect to the time and space, i.e., the temporal ACF and S-CCF depend on the position over the array and on absolute time, respectively. In Section V, we will show that these terms are responsible for the Doppler spectrum drifts along both dimensions. Moreover, the terms that depend on the ratios $v^{\mathrm{S_T}}_c\Delta t/r^{\mathrm{S_T}}_c$ and $\Delta_{pp'}/r^{\mathrm{S_T}}_c$ improve the accuracy of the ST-CCF compared to the conventional stationary MIMO models. Finally, it is worth noting that as the temporal ACFs depend on the pair of antennas A^{T}_p and A^{R}_q considered, they cannot be obtained from the ST-CCFs by setting $\delta_{\mathrm{T}}=\delta_{\mathrm{R}}=0$, but setting $p=p'$ and $q=q'$ in (36)–(43).

2) Large-Scale ST-CCF: Because we assume that the cluster (re)appearance and shadowing processes are independent for simplicity, the large-scale ST-CCF can be separated as the product of the ST-CCF of the cluster (re)appearance processes and that of the shadowing processes as

$$\rho^{\mathrm{SB}}_{\mathrm{LS}}(\delta_{\mathrm{T}},\delta_{\mathrm{R}},\Delta t)=\rho^{\mathrm{SB}}_{\Pi_{qp,c}}(\delta_{\mathrm{T}},\delta_{\mathrm{R}},\Delta t)\cdot\rho^{\mathrm{SB}}_{\gamma_{qp,c}}(\delta_{\mathrm{T}},\delta_{\mathrm{R}},\Delta t).\tag{44}$$

Similarly, since the spatial-temporal cluster (re)appearance process in (31) is expressed as the product of three independent processes, hence the ST-CCF of $\Pi^{\mathrm{SB}}_{qp,c}(t)$ can be calculated as $\rho^{\mathrm{SB}}_{\Pi_c}(\delta_{\mathrm{T}},\delta_{\mathrm{R}},\Delta t)=\rho^{\mathrm{S_T}}_{\Pi_c}(\delta_{\mathrm{T}})\cdot\rho^{\mathrm{S_R}}_{\Pi_c}(\delta_{\mathrm{R}})\cdot\rho^{\mathrm{SB}}_{\Pi_c}(\Delta t)$, where

$$\begin{aligned}
\rho^{\mathrm{S_T}}_{\Pi_c}(\delta_{\mathrm{T}})&=\mathbb{E}[\Pi^{\mathrm{S_T}}_c(\delta_p)\Pi^{\mathrm{S_T}}_c(\delta_{p'})]\\
&=P^{\mathrm{S_T}}_{V,c}\left(P^{\mathrm{S_T}}_{V,c}+P^{\mathrm{S_T}}_{I,c}e^{-\lambda^{\mathrm{S_T}}_{T,c}\delta_{\mathrm{T}}|p-p'|}\right)
\end{aligned}\tag{45}$$

$$\begin{aligned}
\rho^{\mathrm{SB}}_{\Pi_c}(\Delta t)&=\mathbb{E}[\Pi^{\mathrm{SB}}_c(t)\Pi^{\mathrm{SB}}_c(t+\Delta t)]\\
&=P^{\mathrm{SB}}_{V,c}\left(P^{\mathrm{SB}}_{V,c}+P^{\mathrm{SB}}_{I,c}e^{-\lambda^{\mathrm{SB}}_{T,c}|q(\Delta t)|}\right)
\end{aligned}\tag{46}$$

where the receive-side $\rho^{\mathrm{S_R}}_{\Pi_c}(\delta_\mathrm{R})$ can be computed by substituting T by R and p by q in (45). Note that (45) corrects [28, eq. (17)]. Since the total ST-CCF only depends on relative time and antenna elements, the process $\Pi^{\mathrm{SB}}_{qp,c}(\delta_\mathrm{T},\delta_\mathrm{R},t)$ is WSS in these domains. It is worth noting that, since clusters can reappear, the correlation of the (re)apperance processes does not completely vanish for long distances between antenna elements, i.e., the reappearance of clusters introduces additional large-scale correlation.

As the shadowing processes associated to the transmit- and receive-arrays are considered independent, the ST-CCF of $\gamma^{\mathrm{SB}}_{qp,c}(t)$ can be calculated as [32], [33]

$$\begin{aligned}\rho^{\mathrm{SB}}_{\gamma_{qp,c}}(\delta_\mathrm{T},\delta_\mathrm{R},\Delta t) = \exp\left(m^{\mathrm{SB}}_{0,c}+(\sigma^{\mathrm{SB}}_{0,c})^2[1+\rho^{\mathrm{SB}}_{\nu_c}(\Delta t)]\right)\\ \times\exp\left((\sigma^{\mathrm{S_T}}_{0,c})^2[1+\rho^{\mathrm{S_T}}_{\nu_c}(\delta_\mathrm{T})]\right)\\ \times\exp\left((\sigma^{\mathrm{S_R}}_{0,c})^2[1+\rho^{\mathrm{S_R}}_{\nu_c}(\delta_\mathrm{R})]\right)\end{aligned} \tag{47}$$

where it has been defined $m^{\mathrm{SB}}_{0,c}=m^{\mathrm{SB}}_c\ln(10)/10$, $\sigma^{\mathrm{S_T}}_{0,c}=\sigma^{\mathrm{S_T}}_c\ln(10)/10$, and $\sigma^{\mathrm{S_R}}_{0,c}=\sigma^{\mathrm{S_R}}_c\ln(10)/10$. In addition, the terms $\rho^{\mathrm{S_T}}_{\nu_c}(\delta_\mathrm{T})$, $\rho^{\mathrm{S_R}}_{\nu_c}(\delta_\mathrm{R})$, and $\rho^{\mathrm{SB}}_{\nu_c}(\Delta t)$ denote the ACFs of the processes $\nu^{\mathrm{S_T}}_c(\delta_p)$, $\nu^{\mathrm{S_T}}_c(\delta_q)$, and $\nu^{\mathrm{SB}}_c(t)$ defined in (33) and (34), respectively. For the Gaussian correlation model, the ACFs in (47) are [33]

$$\rho^{\mathrm{S_T}}_{\nu_c}(\delta_\mathrm{T}) = e^{-\delta^2_\mathrm{T}|p-p'|^2/(D^{\mathrm{S_T}}_c)^2} \tag{48}$$

$$\rho^{\mathrm{SB}}_{\nu_c}(\Delta t) = e^{-[(v^\mathrm{T}_c)^2+(v^\mathrm{R}_c)^2]\Delta t^2/(D^{\mathrm{SB}}_c)^2}. \tag{49}$$

The parameters $D^{\mathrm{S_T}}_c$ and D^{SB}_c are called the *decorrelation distance* and *decorrelation time* and they are defined as the relative distance and time where the correlations in (48) and (49) become e^{-1}. Since the ACFs in (47)–(49) only depend on relative time and distances, the cluster shadowing process $\gamma^{\mathrm{SB}}_{qp,c}(t)$ is WSS. Finally, as $\rho^{\mathrm{MB}}_{\mathrm{LS}}(\delta_\mathrm{T},\delta_\mathrm{R},\Delta t)$ and $\rho^{\mathrm{L}}_{\mathrm{LS}}(\delta_\mathrm{T},\delta_\mathrm{R},\Delta t)$ are computed analogously, they are omitted.

B. Spatial-Temporal Doppler Frequency Drifts

The non-stationary properties of the channel model result in a spatial-temporal variant Doppler spectrum density. Since the analysis for both SBCs and MBCs is similar and closed-form solutions can only be obtained for MBCs, the MBC case will be presented here. The instantaneous Doppler shift experienced by a ray scattered by a MBC can be computed as the time derivative of the phase $\Delta\Phi^{\mathrm{MB}}_{qp,c,mn}(t)=k_0D^{\mathrm{MB}}_{qp,c,mn}(t)$ in (9) as

$$f^{\mathrm{MB}}_{qp,c,mn}(t)=\frac{1}{2\pi}\cdot\frac{\mathrm{d}\Delta\Phi^{\mathrm{MB}}_{qp,c,mn}(t)}{\mathrm{d}t}=f^{\mathrm{M_T}}_{p,c,m}(t)+f^{\mathrm{M_R}}_{q,c,n}(t) \tag{50}$$

where

$$\frac{f^{\mathrm{M_T}}_{p,c,m}(t)}{f^{\mathrm{M_T}}_{\max}} = \overbrace{\cos\psi^{\mathrm{M_T}}_{1,c,m}}^{\substack{\text{Conventional Tx}\\ \text{Doppler shift}}} + t\cdot\overbrace{\frac{v^{\mathrm{M_T}}_c}{r^{\mathrm{M_T}}_c}\sin^2\psi^{\mathrm{M_T}}_{1,c,m}}^{\text{Temporal drift at Tx}} + \delta_p\cdot\underbrace{\frac{1}{r^{\mathrm{M_T}}_c}Q(\psi^{\mathrm{M_T}}_{1,c,m},\psi^{\mathrm{M_T}}_{2,c,m},\psi^{\mathrm{M_T}}_{3,c})}_{\text{Array drift at Tx}} \tag{51}$$

$$\frac{f^{\mathrm{M_R}}_{q,c,n}(t)}{f^{\mathrm{M_R}}_{\max}} = \overbrace{\cos\psi^{\mathrm{M_R}}_{1,c,n}}^{\substack{\text{Conventional Rx}\\ \text{Doppler shift}}} + t\cdot\overbrace{\frac{v^{\mathrm{M_R}}_c}{r^{\mathrm{M_R}}_c}\sin^2\psi^{\mathrm{M_R}}_{1,c,n}}^{\text{Temporal drift at Rx}} + \delta_q\cdot\underbrace{\frac{1}{r^{\mathrm{M_R}}_c}Q(\psi^{\mathrm{M_R}}_{1,c,n},\psi^{\mathrm{M_R}}_{2,c,n},\psi^{\mathrm{M_R}}_{3,c})}_{\text{Array drift at Rx}} \tag{52}$$

with $f^{\mathrm{M_T}}_{\max}=v^{\mathrm{M_T}}_c/\lambda$, $f^{\mathrm{M_R}}_{\max}=v^{\mathrm{M_R}}_c/\lambda$. The Doppler drift of the LOS component is obtained as

$$\frac{f^{\mathrm{L}}(t)}{f^{\mathrm{L}}_{\max}} = \overbrace{\cos\psi^{\mathrm{L}}_1}^{\substack{\text{Conventional}\\ \text{Doppler shift}}} + t\cdot\overbrace{\frac{v_\mathrm{R}}{r_\mathrm{L}}\sin^2\psi^{\mathrm{L}}_1}^{\text{Temporal drift}} + \delta_p\cdot\overbrace{\frac{1}{r_\mathrm{L}}Q(\psi^{\mathrm{L}}_1,\psi^{\mathrm{L}}_3,\psi^{\mathrm{L}}_5)}^{\text{Array drift at Tx}} - \delta_q\cdot\underbrace{\frac{1}{r_\mathrm{L}}Q(\psi^{\mathrm{L}}_1,\psi^{\mathrm{L}}_2,\psi^{\mathrm{L}}_4)}_{\text{Array drift at Rx}} \tag{53}$$

with $f^{\mathrm{L}}_{\max}=v_\mathrm{R}/\lambda$. The first term in (51) denotes the conventional Doppler shift in stationary MIMO channels [15]–[18], [33]. The second term results in a linear Doppler frequency drift over time whose normalized slope is proportional to $v^{\mathrm{M_T}}_c/r^{\mathrm{M_T}}_c\sin^2\psi^{\mathrm{M_T}}_{1,c,m}$. The third term in (51) represents the effect of the antenna position along the array on the Doppler shift. Similarly to the second term, the Doppler shift experiences a linear drift over the array with a normalized slope proportional to $\delta_\mathrm{T}/r^{\mathrm{M_T}}_cQ(\psi^{\mathrm{M_T}}_{1,c,m},\psi^{\mathrm{M_T}}_{2,c,m},\psi^{\mathrm{M_T}}_{3,c})$. Thus, we can conclude that it is the ratio of the array length (cluster displacement) to the distance between the array and the clusters what determines the contribution of the cluster to the channel non-stationarity over the array (in time domain).

For a uniformly distributed scattering over the 3D sphere, i.e., when $f^\ell_c(\theta^\ell_c,\phi^\ell_c)=\sin(\theta^\ell_c)/4\pi$ with $\ell\in\{\mathrm{M_T},\mathrm{M_R}\}$, we can obtain an explicit solution for the expected value of the Doppler frequency shift as $B^{(1)}_{\mathrm{MB}}=\mathbb{E}[f^{\mathrm{M_T}}_{pm}]+\mathbb{E}[f^{\mathrm{M_R}}_{qn}]$, where the transmit- and receive-side frequency shifts can be computed as $\mathbb{E}[f^{\mathrm{M_T}}_{pm}]=\frac{2}{3}\frac{f^{\mathrm{M_T}}_{\max}}{r^{\mathrm{M_T}}_c}(v^{\mathrm{M_T}}_ct-\delta_p\cos\psi^{\mathrm{M_T}}_{3,c})$ and $\mathbb{E}[f^{\mathrm{M_R}}_{qn}]=\frac{2}{3}\frac{f^{\mathrm{M_R}}_{\max}}{r^{\mathrm{M_R}}_c}(v^{\mathrm{M_R}}_ct-\delta_q\cos\psi^{\mathrm{M_R}}_{3,c})$, respectively. The Doppler frequency spread corresponding to the MBC components can be obtained as $B^{(2)}_{\mathrm{MB}}=(\mathbb{E}[(f^{\mathrm{MB}}_{qp,c,mn})^2]-\mathbb{E}[f^{\mathrm{MB}}_{qp,c,mn}]^2)^{1/2}$ or, equivalently, as $B^{(2)}_{\mathrm{MB}}=(\mathbb{E}[(f^{\mathrm{M_T}}_{p,c,m})^2]+\mathbb{E}[(f^{\mathrm{M_R}}_{q,c,n})^2]-\mathbb{E}[f^{\mathrm{M_T}}_{p,c,m}]^2-\mathbb{E}[f^{\mathrm{M_R}}_{q,c,n}]^2)^{1/2}$ where it has been used the fact that the transmit- and receive-side Doppler frequencies shifts are independent. Finally, the term $\mathbb{E}[(f^{\mathrm{M_T}}_{p,c,m})^2]$ is given by

$$\begin{aligned}\mathbb{E}[(f^{\mathrm{M_T}}_{p,c,m})^2]\\ =\frac{(f^{\mathrm{M_T}}_{\max})^2}{15}\left[5+8\left(\frac{v^{\mathrm{M_T}}_ct}{r^{\mathrm{M_T}}_c}\right)^2-16\left(\frac{v^{\mathrm{M_T}}_ct\delta_p}{r^{\mathrm{M_T}}_c}\right)^2\cos\psi^{\mathrm{M_T}}_{3,c}\right.\\ \left.+\left(\frac{\delta_p}{r^{\mathrm{M_T}}_c}\right)^2\left(1+2\cos\psi^{\mathrm{M_T}}_{3,c}+5\cos^2\psi^{\mathrm{M_T}}_{3,c}\right)\right].\end{aligned} \tag{54}$$

The term $\mathbb{E}[(f^{\mathrm{M_R}}_{q,c,n})^2]$ can be computed analogously and it is omitted here for brevity. The average Doppler frequency shift drifts over the array and in time in a similar fashion

to the individual rays in (51) and (52). Notice that the drift of the average Doppler shift and Doppler spread depends on the orientation of the array with respect to the direction of motion, i.e., the angle $\psi_{3,c}^{\mathrm{M_T}}$. Furthermore, considering short periods of time and small-arrays, i.e., $\{v_c^{\mathrm{M_T}} t, (N_{\mathrm{T}}-1)\delta_{\mathrm{T}}\} \ll r_c^{\mathrm{M_T}}$, both $B_{\mathrm{MB}}^{(1)}$ and $B_{\mathrm{MB}}^{(2)}$ become spatial-temporal invariant as in conventional non-massive MIMO models. Closed-form expressions cannot be obtained for the SBC Doppler drifts because the AoA and AoD are interdependent.

IV. Simulation Model and Statistical Properties

The implementation of the theoretical model is not possible as it requires an infinite number of scatterers. However, it is well known that a finite number of rays can approximate the statistical properties of the theoretical model [33]. As the procedure is the same for SBCs and MBCs, only SBCs will be presented here. The SBC component of the CIR for the simulation model is

$$\hat{h}_{qp,c}^{\mathrm{SB}}(t) = \sqrt{\hat{P}_{qp,c}^{\mathrm{SB}}(t)} \sum_{i=1}^{I_c} \hat{a}_{c,i} e^{j\hat{\Theta}_{c,i}^{\mathrm{SB}}} e^{-jk_0 \hat{D}_{qp,c,i}^{\mathrm{SB}}(t)} \quad (55)$$

where $\hat{a}_{c,i}, \hat{\Theta}_{c,i}^{\mathrm{SB}}, \hat{D}_{qp,c,i}^{\mathrm{SB}}(t)$, and I_c are the simulation model parameters of the small-scale fading process, and $\hat{P}_{qp,c}^{\mathrm{SB}}(t)$ is the cluster's average power of the simulation model. For $\hat{P}_{qp,c}^{\mathrm{SB}}(t)$, the Gaussian processes $\hat{\nu}_{p,c}^{\mathrm{S_T}}(\delta_p)$, $\hat{\nu}_{q,c}^{\mathrm{S_R}}(\delta_q)$, and $\hat{\nu}_c(t)$ contained within $\hat{\gamma}_{qp,c}^{\mathrm{SB}}(t)$ are approximated by a finite number of sinusoids. Due to the similarity of the procedure, only the transmit-side process is presented here. Thus, the process $\hat{\nu}_c^{\mathrm{S_T}}(\delta_p)$ is defined as

$$\hat{\nu}_c^{\mathrm{S_T}}(\delta_p) = \sum_{k=1}^{K_c^{\mathrm{S_T}}} \hat{b}_{c,k}^{\mathrm{S_T}} \cos\left(2\pi \hat{s}_{c,k}^{\mathrm{S_T}} \delta_p + \hat{\Theta}_{c,k}^{\mathrm{S_T}}\right). \quad (56)$$

In the simulation model, it is required to find reasonable values of the parameters $\{\hat{a}_{c,i}, \hat{\theta}_{c,i}^{\mathrm{S_T}}, \hat{\phi}_{c,i}^{\mathrm{S_T}}\}$ in (55) and $\{\hat{b}_{c,k}, \hat{s}_{c,k}\}$ in (56) in order to have a good approximation to the statistical properties of the theoretical model. Aside from the values of $\hat{\Theta}_{c,i}^{\mathrm{SB}}$ and $\hat{\Theta}_{k_c}^{\mathrm{S_T}}$ that are drawn from i.i.d. random variables uniformly distributed over the interval $(0, 2\pi]$, the remaining parameters can be obtained using the corresponding equations of the theoretical model, e.g, $\hat{D}_{qp,c,i}^{\mathrm{SB}}(t)$ in (55) can be obtained using (26). In this paper, a 3D extension of the RSM [29] is used to compute the parameters of the small-scale fading processes, and the MEA [33] is used to compute the parameters of the cluster shadowing processes.

The small-scale ST-CCF of the simulation model for SBCs can be expressed as

$$\hat{\rho}_{\mathrm{SS},qp,c}^{\mathrm{SB}}(\delta_{\mathrm{T}}, \delta_{\mathrm{R}}, \Delta t, t) = \sum_{i=1}^{I_{E,c} I_{A,c}} \hat{a}_{c,i}^2 e^{-jk_0 \hat{\Delta}_{qp,c,i}^{\mathrm{SB}}(\delta_{\mathrm{T}}, \delta_{\mathrm{R}}, \Delta t, t)} \quad (57)$$

where $I_{E,c}$ and $I_{A,c}$ denote the number of rays used in the simulation model in the elevation and azimuth planes, respectively, so the total number of rays in (55) is $I_c = I_{E,c} I_{A,c}$. In the RSM, the theoretical correlation functions in (41) can be approximated as midpoints Riemann sums of finite number of terms [29]. Then, the angular parameters of the simulation model are assumed equally spaced in both the elevation and azimuth planes as $\hat{\theta}_{c,i}^{\mathrm{S_T}} = \pi / I_{E,c} \left(\lceil i / I_{E,c} \rceil - 1/2\right)$ and $\hat{\phi}_{c,i}^{\mathrm{S_T}} = 2\pi / I_{A,c} \left[(i - 1/2) \mod I_{A,c}\right]$, with $i = 1, 2, \ldots, I_{E,c} I_{A,c}$. Here, $\lceil x \rceil$ denotes the least integer greater than or equal to x and $A \mod B$ the remainder after division of A by B. The parameter $\hat{\Delta}_{qp,c,i}^{\mathrm{SB}}(\delta_{\mathrm{T}}, \delta_{\mathrm{R}}, \Delta t, t)$ in (57) can be obtained by plugging $\hat{\theta}_{c,i}^{\mathrm{S_T}}$ and $\hat{\phi}_{c,i}^{\mathrm{S_T}}$ into (11)–(13) and these into (40). Last, the parameters $\hat{a}_{c,i}$ in (57) can be obtained as [29]

$$\hat{a}_{c,i} = \left[\frac{f_c^{\mathrm{S_T}}\left(\hat{\theta}_{c,i}^{\mathrm{S_T}}, \hat{\phi}_{c,i}^{\mathrm{S_T}}\right)}{\sum_{i=0}^{I_{E,c} I_{A,c}} f_c^{\mathrm{S_T}}\left(\hat{\theta}_{c,i}^{\mathrm{S_T}}, \hat{\phi}_{c,i}^{\mathrm{S_T}}\right)} \right]^{1/2}. \quad (58)$$

It is worth noting that the introduction of a new dimension (the elevation angle) into the simulation model increases its complexity compared to its 2D counterpart, as it requires additional terms in the sum of complex exponential functions to represent the elevation component of the rays.

Secondly, the ACF of the SoS process in (56) is given by

$$\hat{\rho}_{\nu_c}^{\mathrm{S_T}}(\delta_{\mathrm{T}}) = \sum_{k=1}^{K_c^{\mathrm{S_T}}} \frac{(\hat{b}_{c,k}^{\mathrm{S_T}})^2}{2} \cos(2\pi \hat{s}_{c,k}^{\mathrm{S_T}} (p - p') \delta_{\mathrm{T}}). \quad (59)$$

For the Gaussian correlation model, the MEA assumes the amplitude of all sinusoids to be $\hat{b}_{c,k}^{\mathrm{S_T}} = \sqrt{2/K_c^{\mathrm{SB}}}$. In addition, the spatial frequencies $\hat{s}_{c,k}^{\mathrm{S_T}}$ can be obtained as [33]

$$\hat{s}_{c,k}^{\mathrm{S_T}} = \frac{1}{\pi D_c^{\mathrm{S_T}}} \mathrm{erf}^{-1}\left(\frac{k - 1/2}{K_c^{\mathrm{S_T}}}\right) \quad (60)$$

where $k = 1, 2, \ldots, K_c^{\mathrm{SB}}$ and $\mathrm{erf}^{-1}(\cdot)$ denotes the inverse error function.

V. Results and Analysis

Henceforth, the scatterers distribution within a cluster is modeled by the VMF distribution, which is defined by the mean elevation angle θ_μ, the mean azimuth angle ϕ_μ, and its concentration parameter $k \geq 0$. The pdf of a VMF random variable is defined in spherical coordinates as [35]

$$f(\theta, \phi) = \frac{k \sin\theta}{4\pi \sinh(k)} \mathrm{e}^{k(\sin\theta_\mu \sin\theta \sin(\phi_\mu - \phi) + \cos\theta_\mu \cos\theta)}. \quad (61)$$

The concentration parameter k determines the angular spread in both azimuth and elevation angles. A high value of k produces a highly concentrated distribution and $k = 0$ results in a uniform distribution on the 3D sphere. In general, the azimuth and elevation angles of the VMF are correlated, with the exception of $k = 0$ and $\theta_\mu = 0$.

A. Small-Scale Statistical Properties of the Channel

In Figs. 2a and 2b, a performance comparison of the plane, parabolic, and spherical wavefronts using the theoretical model is presented. In particular, the absolute values of the transmit-side cluster-level array-variant ACFs and time-variant S-CCFs for a MBC and different values of the VMF concentration parameter are shown. For a fair comparison of the three

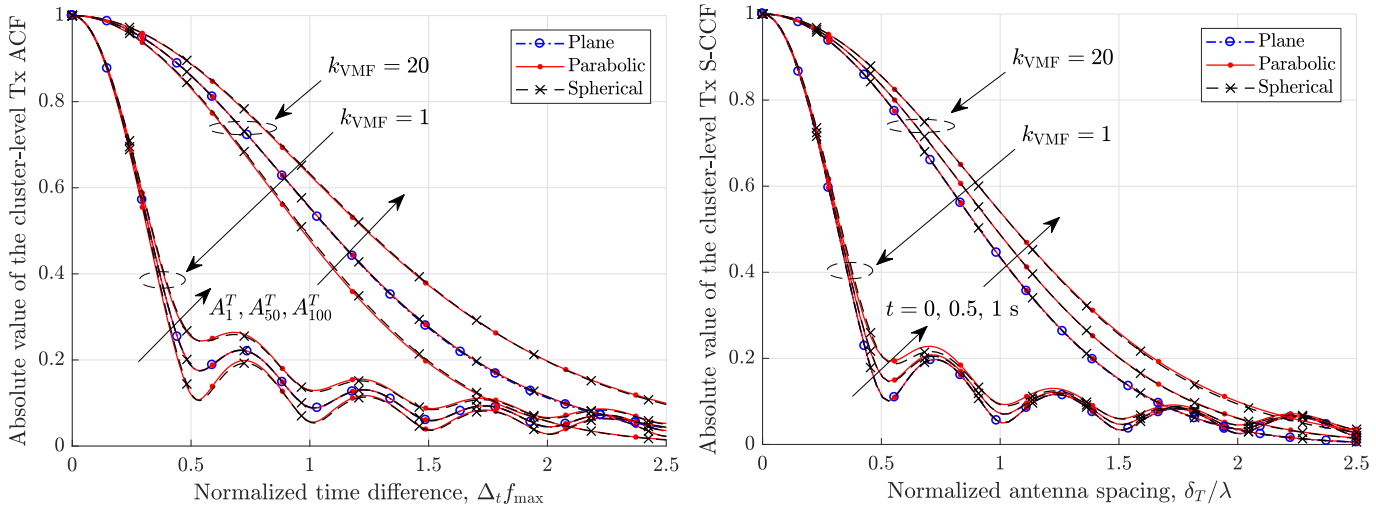

(a) Cluster-level array-variant ACF (b) Cluster-level time-variant S-CCF

Fig. 2. Comparison of the cluster-level transmit-side a) array-variant ACF ($t = 0$) s and b) time-variant S-CCF ($p = 50$) of the theoretical model using plane, parabolic, and spherical wavefronts for different values of VMF k-factor ($f = 2$ GHz, $N_{\text{T}} = 100$, $\delta_{\text{T}} = \lambda/2$, $\beta^{\text{T}} = \pi/2$, $\alpha^{\text{T}} = 0$, $\theta_\mu = 3\pi/4$, $\phi_\mu = \pi/3$, $\zeta_c^{\text{M}_\text{T}} = \pi/2$, $\xi_c^{\text{M}_\text{T}} = \pi/6$, $r_c^{\text{M}_\text{T}} = 30$ m, $v_c^{\text{M}_\text{T}} = 5$ m/s).

wavefronts, it has been set $t = 0$ s and $p = p' = N_{\text{T}}/2$ in (40) to obtain Figs. 2a and 2b, respectively. This enables us to eliminate the influence of absolute time and antenna position on the ACFs and S-CCFs, respectively. Note that as the plane wavefront with static channel parameters cannot capture non-stationary properties of the channel in the spatial or temporal domains, the corresponding results do not show any difference at different antenna elements or time instants. Thus, we only show the results obtained with the plane wavefront at antenna A_{50}^{T} in Fig. 2a and time instant $t = 0$ in Fig. 2b. The temporal ACFs (Fig. 2a) and S-CCFs (Fig. 2b) at the center of the transmit-array ($p = 50$) and time $t = 0$, respectively, show negligible differences for the three different wavefronts as expected. However, unlike the plane wavefront model, the results obtained with the parabolic wavefront demonstrate that it can model non-stationary channels and approximate the corresponding results obtained with the spherical wavefront very well. Also, notice that the array and temporal variations of the ACFs and S-CCFs, respectively, are the result of the cross-products in (40) described in Section III. Finally, it can be observed that the ACF at A_{100}^{T} is higher than that at A_1^{T}. The reason is that, as A_1^{T} is closer to the cluster than A_{100}^{T}, the aparent angular spread at A_1^{T} is higher than that at A_{100}^{T}. Accordingly, as the coherence time, i.e., the region where the ACF is above certain level, is inversely proportional to the angular spread, hence the ACF widens from A_1^{T} to A_{100}^{T}.

In Figs. 3a and 3b, a comparison of the theoretical model, simulation model, and simulation results is presented through the absolute values of the transmit-side cluster-level time-variant ACFs and array-variant S-CCFs, respectively, for a MBC and different values of the VMF concentration parameter. Note that as the CIR is non-stationary and hence non-ergodic, the simulation results have been obtained by averaging over 10^4 realizations of the correlation functions. Unlike Figs. 2a and 2b, these results demonstrate temporal and spatial non-stationarity through the ACFs and S-CCFs, respectively. It is worth noting the very good agreement between theoretical and simulation results obtained through the extended 3D RSM in non-stationary conditions. In our study, we have verified that the 3D RSM outperforms the Monte Carlo method in the approximation of the ACFs and S-CCFs in more than one order of magnitude using $N_c^{\text{M}_\text{T}} = 8$ and $M_c^{\text{M}_\text{T}} = 16$ in the EAoD and AAoD, respectively.

On the other hand, whereas the accuracy of the parabolic wavefront has already been assessed, the benefits in terms of computational complexity have not been shown yet. In order to provide an estimation of the computational gain, we used the ratio of the average simulation time of calculating plane, parabolic, and spherical wavefronts under the condition that all the rest parameters in the simulations were kept the same. To minimize the influence of the selected parameters on the results, we employed random parameters in every simulation and we averaged the computation time over many realizations (10^4). The ratios of the average computation time of computing plane, parabolic, and spherical wavefronts obtained are: $T_{\text{plane}}/T_{\text{spherical}} = 0.06$, $T_{\text{plane}}/T_{\text{parabolic}} = 0.35$, $T_{\text{parabolic}}/T_{\text{spherical}} = 0.17$. The plane wavefront is the most efficient but it cannot capture non-stationary properties of the channel. Remarkably, the average computation time of the parabolic wavefront is 17% of the average time required by the spherical wavefront, which demonstrates the efficiency of the proposed approach.

B. Large-Scale Statistical Properties of the Channel

The large-scale characteristics of the proposed model were validated by employing the outdoor measurements reported in [9] and [12]. Gao *et al.* [9] studied the distribution of the VRs length along the array by setting a 128-element virtual ULA spanning 7.5 m on the rooftop of a building in a semi-urban environment. In a similar setting [11] [12], Payami et al. studied the array-variant RMS DS by setting a virtual ULA composed by 128 omnidirectional antenna

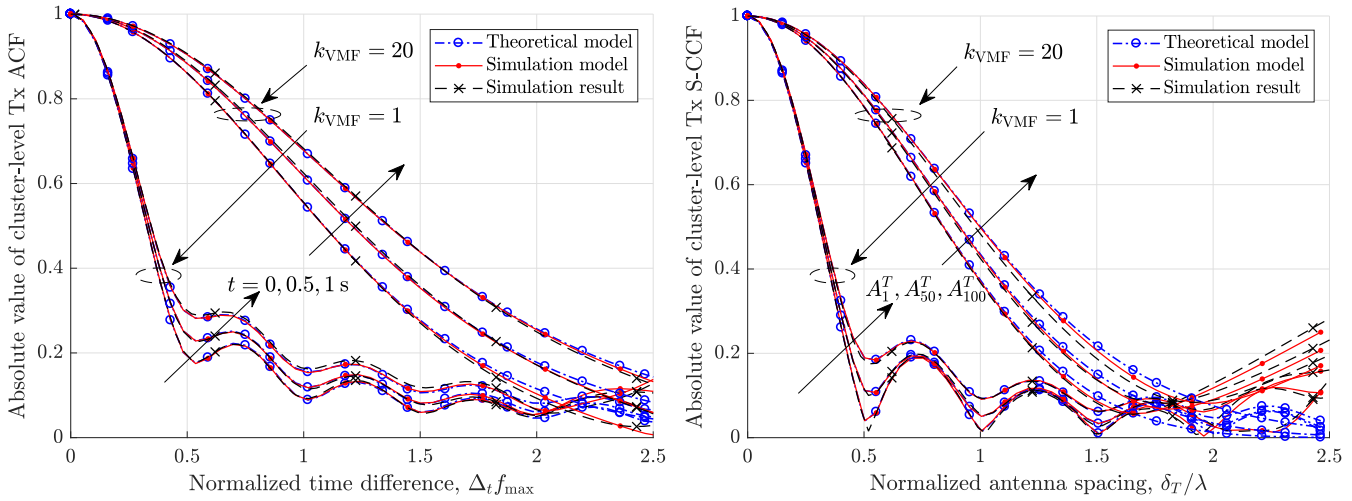

(a) Cluster-level time-variant ACF (b) Cluster-level array-variant S-CCF

Fig. 3. Comparison of the cluster-level transmit-side a) time-variant ACFs ($p = 50$) and b) array-variant S-CCFs ($t = 0$) of the theoretical model, simulation model, and simulation results for different values of VMF k-factor ($f = 2$ GHz, $N_c^{\text{M}_\text{T}} = M_c^{\text{M}_\text{T}} = 15$, $N_\text{T} = 100$, $\delta_\text{T} = \lambda/2$, $\beta^\text{T} = \pi/2$, $\alpha^\text{T} = 0$, $\theta_\mu = 3\pi/4$, $\phi_\mu = \pi/3$, $\zeta_c^{\text{M}_\text{T}} = \pi/2$, $\xi_c^{\text{M}_\text{T}} = \pi/6$, $r_c^{\text{M}_\text{T}} = 30$ m, $v_c^{\text{M}_\text{T}} = 5$ m/s).

elements spaced half wavelength. In both cases, the measurements were performed in LOS and NLOS conditions at a central frequency of 2.6 GHz with a signal bandwidth of 50 MHz.

For the simulation results, if some channel parameters, e.g., carrier frequency, antenna separation, and number of antennas, were provided in the measurements (such as in [9] and [12]), they were directly employed in our simulations. The rest channel model parameters, e.g., $\lambda_{V,c}$, $\lambda_{I,c}$, σ_c, and D_c, were then estimated using an optimization algorithm in order to fit the statistical properties of the channel model to those of the measurement data. In the estimation process, random initial values of those parameters were first generated. Then, the average root mean square error of the simulation and measurement results was minimized by optimizing the values of those parameters in an iterative process. The following simulation results, e.g, cumulative distribution functions (CDFs), were obtained by using the Monte Carlo method, i.e., performing multiple simulation runs (10^4). We employed 20 clusters per simulation run and the number of sinusoids per cluster to generate the shadowing processes was 25. Notice that $\lambda_{I,c}$ and $\lambda_{V,c}$, σ_c, and D_c are assumed to be equal for every cluster.

In Fig. 4, the CDFs of the measured and simulated VRs' length over the array are presented for different values of the visibility rates. The VRs inside the array were selected for comparison as their information is complete and reliable [9]. Although the measurement and simulation curves for $\lambda_{I,c} = \lambda_{V,c} = 0.5$ m^{-1} are in good agreement for most of the range, there are discrepancies between these curves for low values of the VR's length, which can be explained due to the lack of reliable information for short VRs. Note that as the maximum length of a VR that can be measured over a ULA is equal to the length of the array (see [9, Fig. 6(b) and (c)]), we limited the maximum length of VRs to the ULA length. As a result, a discontinuity occurs in the CDF at a VR length of about 7.5 m for $\lambda_{I,c} = \lambda_{V,c} = 0.1$. In this case, whereas

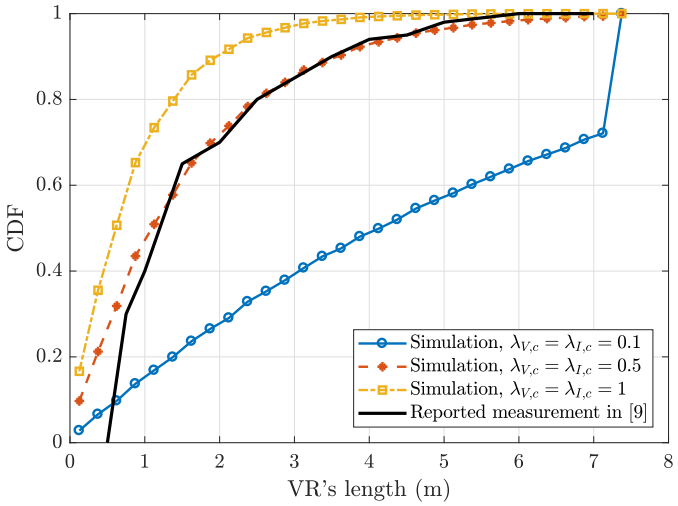

Fig. 4. Measured [9] and simulated CDFs of the clusters' VRs lengths over the array ($f = 2.6$ GHz, $N_\text{R} = 128$, $\delta_\text{R} = \lambda/2$).

approximately 70% of VRs are strictly shorter than 7.5 m, 30% are longer than or equal to 7.5 m. Generally, it can be stated that the lower the cluster disappearance rate, the higher the percentage of clusters visible over the entire ULA and the larger the discontinuity.

In the VR approach for massive MIMO arrays developed in [9], the slopes of the clusters' average power variations along the array were employed to model cluster-level large-scale fading. These slopes were estimated in a least-squares sense in decibel domain. In Fig. 5, the CDFs of the slopes simulated and estimated from measurements are presented for comparison purposes. Note that to estimate the values of the slopes by simulations, we kept fixed the values of the visibility rates $\lambda_{I,c} = \lambda_{V,c} = 0.5$ m^{-1} previously obtained (see Fig. 4). It is worth noting that larger standard deviations of the clusters power σ_c tend to increase the spread of the slopes, whereas larger decorrelation distances produce the opposite

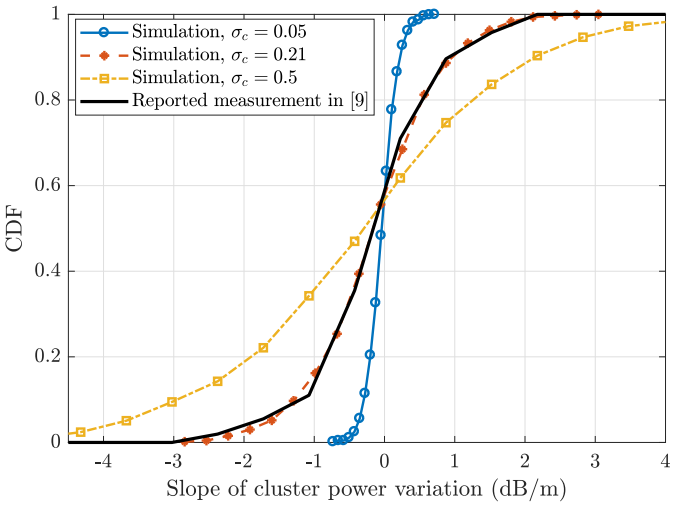

Fig. 5. Measured and simulated CDFs of slopes of the cluster's power variations along the array for different values of the standard deviation of the clusters' average power ($f = 2.6$ GHz, $\lambda_{I,c} = \lambda_{V,c} = 0.5$ m^{-1}, $D_c = 1.23$ m, $N_{\mathrm{R}} = 128$, $\delta_{\mathrm{R}} = \lambda/2$).

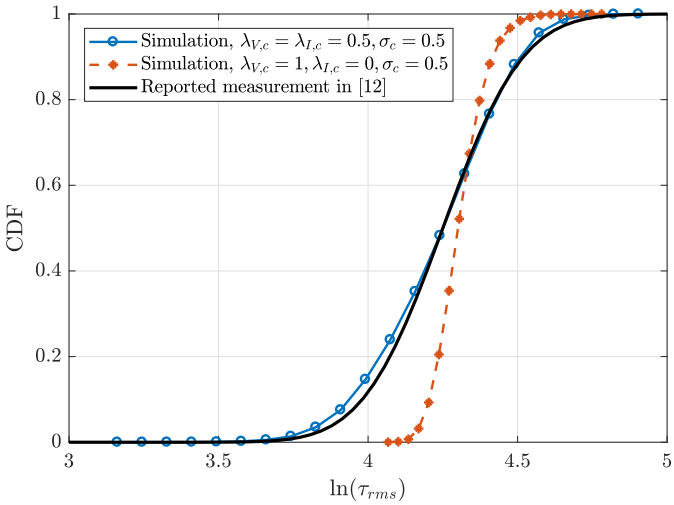

Fig. 6. Comparison of the simulated and estimated [12] CDFs of the array-variant RMS DS for different values of the (re)apperance rates and standard deviation of the clusters' average power ($f = 2.6$ GHz, $N_{\mathrm{R}} = 128$, $\delta_{\mathrm{R}} = \lambda/2$, $D_c = 1.23$ m).

effect. Moreover, it should be remarked that the area mean has little or no impact on the CDFs of the slopes.

Caused by the (re)appearance of clusters and smooth evolution of the clusters' average power along the array, variations of the RMS DS as reported in [12] need to be captured by massive MIMO channel models. For that purpose, in Fig. 6 we present a comparison of the simulated and measured CDFs of the RMS DS over the array. The simulation results correspond to different values of the appearance rates and clusters' average power standard deviations. Whereas shadowing of clusters results in variations of the DS, adding both cluster (re)appearance and shadowing enables us to model such variations of the DS more accurately.

VI. Conclusion

In this paper, we have developed and studied a novel 3D non-stationary wideband theoretical channel model and a corresponding simulation channel model for massive MIMO communication systems. Firstly, a new efficient and accurate way of capturing spatial-temporal non-stationary properties of the channel through parabolic wavefronts has been proposed. We have demonstrated that the parabolic wavefront is sufficiently flexible and accurate to model the statistical properties of the channel with reduced computational complexity. Moreover, the relationship between non-stationary properties of the channel, e.g., time- and array-variant ST-CCFs and Doppler frequency drifts, and the distance between the arrays and clusters has been shown. Secondly, non-stationary properties of the channel have also been modeled through cluster-level evolution processes in space and time domains. A comparison of simulation results and measurements have validated the spatial-temporal cluster (re)appearance and lognormal shadowing processes in order to approximate key statistical properties of the channel such as the length of the clusters' VRs, the array-variant cluster power and array-variant DS. Finally, a 3D extension of the RSM for parameters computation has been proposed and validated through simulations.

References

[1] E. G. Larsson, O. Edfors, F. Tufvesson, and T. L. Marzetta, "Massive MIMO for next generation wireless systems," *IEEE Commun. Mag.*, vol. 52, no. 2, pp. 186–195, Feb. 2014.

[2] E. Björnson, E. G. Larsson, and T. L. Marzetta, "Massive MIMO: Ten myths and one critical question," *IEEE Commun. Mag.*, vol. 54, no. 2, pp. 114–123, Feb. 2016.

[3] C.-X. Wang *et al.*, "Cellular architecture and key technologies for 5G wireless communication networks," *IEEE Commun. Mag.*, vol. 52, no. 2, pp. 122–130, Feb. 2014.

[4] C. Shepard *et al.*, "Argos: Practical many-antenna base stations," in *Proc. ACM MOBICOM*, Istanbul, Turkey, 2012, pp. 53–64.

[5] J. Vieira *et al.*, "A flexible 100-antenna testbed for Massive MIMO," in *Proc. IEEE GLOBECOM*, Austin, TX, USA, Dec. 2014, pp. 287–293.

[6] P. Harris *et al.*, "LOS throughput measurements in real-time with a 128-antenna massive MIMO testbed," in *Proc. IEEE GLOBECOM*, Washington, DC, USA, Dec. 2016, pp. 1–7.

[7] D. Tse and P. Viswanath, *Fundamentals of Wireless Communication*, 1st ed. Cambridge, U.K.: Cambridge Univ. Press, 2005.

[8] X. Gao, F. Tufvesson, O. Edfors, and F. Rusek, "Measured propagation characteristics for very-large MIMO at 2.6 GHz," in *Proc. IEEE ASILOMAR*, Pacific Grove, CA, USA, Nov. 2012, pp. 295–299.

[9] X. Gao, F. Tufvesson, and O. Edfors, "Massive MIMO channels—Measurements and models," in *Proc. IEEE ASILOMAR*, Pacific Grove, CA, USA, Nov. 2013, pp. 280–284.

[10] W. Li, L. Liu, C. Tao, Y. Lu, J. Xiao, and P. Liu, "Channel measurements and angle estimation for massive MIMO systems in a stadium," in *Proc. IEEE ICACT*, Seoul, South Korea, Jul. 2015, pp. 105–108.

[11] S. Payami and F. Tufvesson, "Channel measurements and analysis for very large array systems at 2.6 GHz," in *Proc. IEEE EUCAP*, Prague, Czech Republic, Mar. 2012, pp. 433–437.

[12] S. Payami and F. Tufvesson, "Delay spread properties in a measured massive MIMO system at 2.6 GHz," in *Proc. IEEE PIMRC*, London, U.K., Sep. 2013, pp. 53–57.

[13] X. Gao, O. Edfors, F. Rusek, and F. Tufvesson, "Massive MIMO performance evaluation based on measured propagation data," *IEEE Trans. Wireless Commun.*, vol. 14, no. 7, pp. 3899–3911, Jul. 2015.

[14] X. Gao, O. Edfors, F. Tufvesson, and E. G. Larsson, "Massive MIMO in real propagation environments: Do all antennas contribute equally?" *IEEE Trans. Commun.*, vol. 63, no. 11, pp. 3917–3928, Nov. 2015.

[15] *Spatial Channel Model for Multiple-Input Multiple-Output (MIMO) Simulations*, document 3GPP T.S. 25.996, 2012.

[16] J. Meinilä *et al.*, "WINNER+ final channel models," WINNER+, Tech. Rep. D5.3 V1.0, Jun. 2010.

[17] *Guidelines for Evaluation of Radio Interface Technologies for IMT-Advanced*, document ITU-R M.2135, Geneva, Switzerland, 2008.

[18] R. Verdone and A. Zanella, Eds., *Pervasive Mobile and Ambient Wireless Communications: COST Action 2100*, 1st ed. London, U.K.: Springer, 2011.
[19] *Study on 3D Channel Model for LTE, Version 12.4.0*, document TR 36.873, 3rd Generation Partnership Project (3GPP), 2017.
[20] C.-X. Wang, S. Wu, L. Bai, X. You, J. Wang, and C.-L. I, "Recent advances and future challenges for massive MIMO channel measurements and models," *Sci. China Inf. Sci.*, vol. 59, no. 2, pp. 1–16, Feb. 2016.
[21] S. Jaeckel, L. Raschkowski, K. Börner, and L. Thiele, "QuaDRiGa: A 3-d multi-cell channel model with time evolution for enabling virtual field trials," *IEEE Trans. Antennas Propag.*, vol. 62, no. 6, pp. 3242–3256, Jun. 2014.
[22] M. Peter *et al.*, "Measurement campaigns and initial channel models for preferred suitable frequency ranges," mmMAGIC, Tech. Rep. D2.1 V1.0, 2016.
[23] S. Wu, C. X. Wang, H. Haas, E. H. M. Aggoune, M. M. Alwakeel, and B. Ai, "A non-stationary wideband channel model for massive MIMO communication systems," *IEEE Trans. Wireless Commun.*, vol. 14, no. 3, pp. 1434–1446, Mar. 2015.
[24] S. Wu, C.-X. Wang, M. Aggoune, M. M. Alwakeel, and Y. He, "A non-stationary 3-D wideband twin-cluster model for 5G massive MIMO channels," *IEEE J. Sel. Areas Commun.*, vol. 32, no. 6, pp. 1207–1218, Jun. 2014.
[25] A. Maltsev *et al.*, "Channel modeling and characterization," MiWEBA, Tech. Rep. D5.1 V1.0, Jun. 2014.
[26] A. Maltsev *et al.*, *Channel Models for 60 GHz WLAN Systems*, Standard IEEE 802.11ad 09/0334r8, Jan. 2010.
[27] *METIS Channel Models*, document ICT-317669 METIS Project, D1.4 v3, Jun. 2015.
[28] C. F. López, C.-X. Wang, and R. Feng, "A novel 2D non-stationary wideband massive MIMO channel model," in *Proc. IEEE CAMAD*, Toronto, ON, Canada, Oct. 2016, pp. 207–212.
[29] C. A. Gutiérrez and M. Pätzold, "The Riemann sum method for the design of sum-of-cisoids simulators for Rayleigh fading channels in non-isotropic scattering environments," in *Proc. IEEE ICUMT*, Saint Petersburg, Russia, Oct. 2009, pp. 1–5.
[30] T. Zwick, C. Fischer, D. Didascalou, and W. Wiesbeck, "A stochastic spatial channel model based on wave-propagation modeling," *IEEE J. Sel. Areas Commun.*, vol. 18, no. 1, pp. 6–15, Jan. 2000.
[31] A. Papoulis, *Probability, Random Variables and Stochastic Processes*, 4th ed. New York, NY, USA: McGraw-Hill, 2002.
[32] M. Pätzold and V. D. Nguyen, "A spatial simulation model for shadow fading processes in mobile radio channels," in *Proc. IEEE PIMRC*, Barcelona, Spain, Sep. 2004, pp. 1832–1838.
[33] M. Pätzold, *Mobile Radio Channels*, 2nd ed. West Sussex, U.K.: Wiley, 2012.
[34] X. Cai and G. B. Giannakis, "A two-dimensional channel simulation model for shadowing processes," *IEEE Trans. Veh. Technol.*, vol. 52, no. 6, pp. 1558–1567, Nov. 2003.
[35] K. Mardia and P. E. Jupp, *Directional Statistics*. Hoboken, NJ, USA: Wiley, 2000.

Carlos F. López received the B.Sc. and M.Sc. degrees in telecommunications engineering from the Technical University of Madrid, Spain, in 2011 and 2015, respectively. He is currently pursuing the Ph.D. degree with Heriot-Watt University, Edinburgh, U.K.

In 2011, he was a Research Engineer with the Radio Communication Research Group, Technical University of Madrid, where he led the design and development of simulation tools for wireless channel modeling in 4G/LTE mobile communications networks, and he carried out measurement campaigns for wireless channel characterization using broadband communication systems in Madrid Metro facilities. In 2015, he was a Research Engineer with the Radio Access Group, Telefónica Research and Development, Madrid, Spain, where he was involved in the simulation of 5G wireless communication systems including massive multiple-input multiple-output (MIMO) and millimeter-wave (mm-wave) technologies, novel multiplexing techniques using massive MIMO, and the testing of adaptive channel coding schemes via link-to-system models. Since 2015, he has been a Research Associate with Heriot-Watt University. His research interests include wireless channel measurements, modeling, and simulation, massive MIMO systems, mm-wave wireless communications, and spatial modulation.

Cheng-Xiang Wang (S'01–M'05–SM'08–F'17) received the B.Sc. and M.Eng. degrees in communication and information systems from Shandong University, China, in 1997 and 2000, respectively, and the Ph.D. degree in wireless communications from Aalborg University, Denmark, in 2004.

He was a Research Assistant with the Hamburg University of Technology, Hamburg, Germany, from 2000 to 2001, a Research Fellow at the University of Agder, Grimstad, Norway, from 2001 to 2005, and a Visiting Researcher with Siemens AG-Mobile Phones, Munich, Germany, in 2004. He has been with Heriot-Watt University, Edinburgh, U.K., since 2005, and became a Professor in wireless communications in 2011. He is also an Honorary Fellow at The University of Edinburgh, U.K., a Chair Professor of Shandong University, and a Guest Professor of Southeast University, China. He has co-authored two books, one book chapter, and over 320 papers in refereed journals and conference proceedings. His current research interests include wireless channel measurements/modeling and (B)5G wireless communication networks, including green communications, cognitive radio networks, high mobility communication networks, massive MIMO, millimeter wave communications, and visible-light communications.

Dr. Wang is a fellow of the IET and HEA. He received nine Best Paper Awards from IEEE GLOBECOM 2010, IEEE ICCT 2011, ITST 2012, IEEE VTC 2013-Spring, IWCMC 2015, IWCMC 2016, IEEE/CIC ICCC 2016, and WPMC 2016. He has served as a technical program committee (TPC) member, the TPC chair, and a general chair for over 80 international conferences. He has served as an editor for nine international journals, including the IEEE TRANSACTIONS ON WIRELESS COMMUNICATIONS from 2007 to 2009, the IEEE TRANSACTIONS ON VEHICULAR TECHNOLOGY since 2011, and the IEEE TRANSACTIONS ON COMMUNICATIONS since 2015. He was the Lead Guest Editor of the IEEE JOURNAL ON SELECTED AREAS IN COMMUNICATIONS Special Issue on Vehicular Communications and Networks. He was also a Guest Editor of the IEEE JOURNAL ON SELECTED AREAS IN COMMUNICATIONS Special Issue on Spectrum and Energy Efficient Design of Wireless Communication Networks and Special Issue on Airborne Communication Networks, and a Guest Editor of the IEEE TRANSACTIONS ON BIG DATA Special Issue on Wireless Big Data. He is recognized as a Web of Science 2017 Highly Cited Researcher.